LBL-11428

Lawrence Berkeley Laboratory
UNIVERSITY OF CALIFORNIA

Lectures given at the XIII Masurian School of Nuclear Physics, "Nuclear Structure Study by Means of Nuclear Reactions", Mikolajki, Poland, September 1-13, 1980

SPIN AND ISOSPIN FLUCTUATIONS IN HEAVY ION COLLISIONS AND THEIR DEPENDENCE UPON THE SHAPE OF THE DINUCLEAR COMPLEX

Luciano G. Moretto

August 1980

Prepared for the U.S. Department of Energy under Contract W-7405-ENG-48

Lectures given at the XIII Masurian School
of Nuclear Physics, "Nuclear Structure Study
by Means of Nuclear Reactions," Mikolajki, Poland
Sept. 1-13, 1980

SPIN AND ISOSPIN FLUCTUATIONS IN HEAVY ION COLLISIONS AND THEIR DEPENDENCE UPON THE SHAPE OF THE DINUCLEAR COMPLEX

Luciano G. Moretto

Nuclear Science Division
Lawrence Berkeley Laboratory
University of California
Berkeley, CA 94720

ABSTRACT

The relevance of higher multipoles of giant isovector modes in the charge distribution of deep inelastic fragments is discussed and found to depend strongly on mass asymmetry. The sources of angular momentum fluctuations are investigated. Quantal effects are considered as well as effects arising from non-equilibrium and equilibrium statistical fluctuations. A model based upon equilibrium statistical mechanics is considered in detail and used to predict both 2^{nd} moments of the angular momentum distributions and the angular momentum misalignment. Analytical expressions are derived to calculate the angular distributions of sequentially emitted particles, fission fragments, as well as gamma rays in terms of the angular momentum misalignment. Recent data on the angular distributions of sequential alphas, fission and gamma rays are analyzed in terms of the model.

1. INTRODUCTION

Western culture, of which I may venture to speak with a minimum of competence, is characterized by a series of archetypal hang-ups that keep recurring, though disguised in elusive, ever-shifting ways. As a case in point, one may consider the hang-up of symmetry in general, and of spherical symmetry in particular. The Greeks bear the responsibility of having invented it, and Plato, in particular, has been the major villain by introducing it to learned societies and in Academia. And it so happened that heaven and earth became rigorously spherical, and remained such for at least two thousand years. Copernicus himself could not break away from tradition: he kept the circles although he quietly rearranged them somewhat. Galileo, being Italian, could not keep quiet, and paid for it (actually he did not pay, he was given free room and board for the rest of his life). Kepler found, to his own grief, that planets went around in ellipses. But the shadow of Plato was keeping good guard, and, as it is well-known, forced Kepler to fit the orbits within the platonic solids. That is how supersymmetries made their appearance in physics.

Jumping to the present, one would say that particle physicists are the most platonic brand of scientists. All they seem to want to do, is to play around with group theory, as they see symmetries everywhere. And when nature does not comply, so much the worse for nature. It is clear that old symmetries never die, they only get broken (spontaneously) to provide physicists with a job and steady income.

Nuclear physics is not an exception to the rule. Again the ontogenesis of nuclear physics repeats the phylogenesis of science at

large. We all know, after all, that nuclei were born perfectly spherical too. So they remained for a while, but eventually some of them had to be allowed to deform, discretly, so that they could be handled in a spherical basis. The major violation of spherical symmetry occurred with the discovery of fission, with disastrous consequences. Aside from fission on which, as we said, we may not have adequate control, we have been confined in our studies to spherical or near spherical nuclei until the advent of heavy ions. Granted that we have not run into any nucleus that is not spherical or near-spherical in its ground state as yet, nonetheless, we have produced relatively long-lived transient structures which are a far cry from sphericity. These nuclei with lumps and bumps can be studied in reasonable detail, certainly in their equilibrium and non equilibrium statistical properties and, at times, even in their spectroscopy (as in quasi molecular states).

So it seems that we have finally broken away from platonic tradition and we are now ready for the exhilaration of baroque freedom. Consequently, while it lasts, and the yearning for the beautiful simplicity of symmetries does not force us yet to study the quark structure of the deuteron or of the alpha particle, let us study and enjoy the bizarre properties of the even more bizarre "intermediate complex," or dinucleus which is formed in deep inelastic collisions.

We shall consider two aspects of the dinuclear properties, namely isospin and rotational degrees of freedom.

Isospin degrees of freedom control the distribution of the neutron-to-proton ratios in the deep inelastic fragments. The connection with

giant isovector modes of the intermediate complex is quite tantalizing although not proven as yet. However, on the chance that such a connection exists, it is difficult to resist the temptation to speculate on the possible information that can be extracted from charge distributions, like the strength function of these giant modes at high excitation energy and perhaps for high multipolarity.

Rotational and angular momentum bearing degrees of freedom are numerous and their effect is very pervasive. One could almost argue that more than half of the phenomenology of heavy ion reactions is more or less directly connected with them. The beautiful and varied results that have been obtained through a number of fancy techniques, and their theoretical interpretation, touch upon a great deal of high spin nuclear physics that has been recently developed for compound nuclei. In particular, the ability to control the spin alignment of the produced fragments to a good degree, opens up and a whole new field of study for highly excited high spin aligned nuclei.

2. ISOPIN FLUCTUATIONS

The mass asymmetry degree of freedom is known to be the slowest to relax among the collective modes excited in heavy ion reactions, while the charge equilibration appears to occur on a faster time-scale.

Information regarding the isospin fluctuations in the intermediate complex can be obtained from the isobaric charge distributions.[1] The observed distributions are Gaussian and the fluctuations can be characterized by the variance σ^2 of the distributions.

An immediate, though not necessarily warranted approximation has been made by assuming that only the lower isovector multipole, (corresponding to the E1 mode, like in the giant dipole resonance) is involved in the charge fluctuations.[1,2,3]

If the phonon energy of the dipole mode is $\hbar\omega$ and the stiffness constant is c, then two limiting situations do arise.

The first corresponds to the case in which the collective mode is weakly coupled to the other modes. In this limit and for $T \ll \hbar\omega$ one would expect only ground state quantal fluctuations for which

$$\sigma^2 = \frac{\hbar\omega}{2c} \tag{1}$$

On the other hand, if $T \gg \hbar\omega$ (always weak coupling) or if the collective mode is so strongly coupled to the continuum that its strength function is very spread out, one obtains the classical limit in which the fluctuations depend only upon the temperature T:

$$\sigma^2 = \frac{T}{c} \tag{2}$$

It is difficult to argue a priori for either of the two possibilities. If during the decay stage, the decoupling from adiabaticity occurs while the neck between the two fragments is still very large, and the weak coupling limit holds, one would expect $\hbar\omega \approx 96/d$ MeV where d is the distance between the two fragment centers. In this case $\hbar\omega \gg T$ in most

reactions and large fluctuations, of the order of $\sigma^2 \simeq 1\ e^2$ should be observed, independent of excitation energy. On the other hand, if the strong coupling limit is prevailing, one would expect fluctuations of perhaps $\sigma^2 \simeq 0.3\ e^2$ and increasing with excitation energy.

Extraordinarily enough, both situations[2,3] are observed in various reactions as illustrated in Figs. 1 and 2. While this problem, in view of the puzzling experimental data, is in a state of substantial confusion, we believe that one should exercise some caution in the assumptions which are commonly made, tacitly or not. In particular the allegedly contradictory findings of large and small charge fluctuations at large and small mass asymmetries respectively, and the related attempts to infer the relevant E1 phonon energies, suffer from a lack of systematic understanding of the role played by the various giant isovector modes in the charge fluctuations.

We are proposing here a simple model[4] that, while it may not be adequately realistic, is complete and points out important facts which have been overlooked.

We shall disregard the extremely important dynamical aspects of the problem[5] and assume that the particular shapes considered in our model just precede the rapid division into two fragments. In particular, let us consider the axial isovector modes in a cylinder of length 2a, radius r, which is suddenly split at a distance b from one of the

bases. The standing isovector waves are clearly trigonometric functions and the boundary conditions require them to be cosine functions.

According to the Steinwedel-Jensen model, the fluctuation of the charge density for the mode of order n is:

$$\rho_z = -\frac{1}{2}\rho_z^o a_n \cos k_n x \qquad (3)$$

where ρ_z^o is the equilibrium charge density, a_n is the amplitude of the mode, x is the distance along the cylinder axis from one of the bases, and the wave number k_n is given by $k_n = (\pi/2a)\, n$. The frequency of each mode is given by $\omega_n = k_n u$, where

$$u = \left(\frac{8X}{m}\,\frac{ZN}{A^2}\right)^{1/2} \simeq 0.21c \qquad (4)$$

is the isospin sound velocity, which is assumed to be frequency-independent; X is the liquid drop symmetry energy coefficient and m is the nucleon mass.

If we cut the cylinder at b, we can define the charge excess of one of the fragments by the relation:

$$Z_n = \frac{-1}{2}\rho_z^o a_n \pi r^2 \int_0^b \cos k_n x\,dx = \frac{-a_n Z}{2\pi}\,\frac{\sin[n\pi Q]}{n} \qquad (5)$$

where the degree of symmetry $Q = b/2a$.

Since the transformation from the coordinate x to the variable Z_n does not involve time, we can conclude that Z_n oscillates harmonically, because a_n does. Classically, for a fixed value of Q, each Z_n is a separate normal mode.

Let us now determine the stiffness constant of each of these normal modes; we know the frequency already. We can do this by calculating the potential energy (disregarding Coulomb forces for the moment):

$$V = X \int \frac{(\rho_n - \rho_z)^2}{\rho_0} d\tau = \frac{X a_n^2}{8} A \qquad (6)$$

and substituting the amplitude a_n obtained from Eq. (5) into Eq. (6). The potential energy is indeed quadratic in Z_n: $V = (1/2)\, c_n Z_n^2$ with

$$c_n = X \frac{A}{Z^2} \pi^2 \frac{n^2}{\sin^2[n\pi Q]} \qquad (7)$$

Note that the stiffness constant depends strongly on n. For any n, some of the charge fluctuations average out and do not contribute to the fragment charge fluctuation; this is all the more true the larger n is, since it takes more energy to displace a given amount of charge into any given fragment. Even for the lowest mode (n = 1), some of the energy goes into polarizing the fragments rather than displacing charge. This is to be contrasted with the standard way in which c has been calculated

so far, using a potential which neglects fragment polarization: $V = V_{LD}(1) + V_{LD}(2) + V_C(1,2)$ where $V_{LD}(1)$ and $V_{LD}(2)$ are the liquid drop energies of two touching spheres and $V_C(1,2)$ is their Coulomb repulsion. The stiffness constant follows as:

$$c_{LD} = \left.\frac{\partial^2 V}{\partial Z_1^2}\right|_{\text{constant A}} \tag{8}$$

where Z_1 is the charge of one of the fragments. In Fig. 3, c_1 and c_{LD} can be compared as a function of Q. The large error introduced by neglecting the fragment polarization is obvious, especially at large asymmetries.

Notice also that for the special values of Q for which $\sin[n\pi Q]$ is zero, the stiffness constant is infinite; no matter how much work is done, no charge displacement arises. This is true in particular at symmetry ($Q = 1/2$), where none of the even modes contribute to displacement.

After having identified the Z_n as classical normal modes, we can immediately quantize them. For each mode we obtain a phonon energy

$$\hbar\omega_n = \frac{\hbar u \pi}{2a} n \tag{9}$$

These phonon energies are very large even for the lowest modes, so that the limit $T/\hbar\omega_n \ll 1$ is typically encountered (T = nuclear temperature) and only zero-point fluctuations need to be considered.

For each mode n, the zero-point charge width is given by

$$\sigma_n^2 = \frac{\hbar\omega_n}{2C_n} = \sigma_1^2(\text{symmetry})\ \frac{\sin^2[n\pi Q]}{n} \tag{10}$$

From Fig. 3 and Eq. (8), one expects these widths to be smaller at large asymmetries than those calculated neglecting fragment polarization, and experiments[2,3] seem to indicate such an effect. The contribution of the n^{th} mode to σ^2 goes like 1/n, so that the contribution of the higher modes becomes less relevant the higher n is. However, the total charge width in this model diverges logarithmically:

$$\sigma^2 = \sigma_1^2(\text{symmetry})\ \sum \frac{\sin^2[n\pi Q]}{n} \tag{11}$$

This is not surprising, because we are assigning an infinite number of degrees of freedom to a system of finite particle number. Furthermore, it is likely that the higher-frequency modes "drown" in the doorway states directly coupled to them, as illustrated in[1] thus removing the collectiveness from the respective degrees of freedom. The location of the cutoff in n, or even whether a fully quantal treatment is warranted for the lowest mode, is most relevant.

The wavelength of the oscillations cannot be much smaller than the diameter of a nucleon; thus one obtains an upper limit for the cutoff in n: $n_{max} = 4.8\ A^{1/3}$ for $\lambda_{min} = 1.5$ fm.

A very important feature of this model is that the role of each mode strongly depends upon the asymmetry of the system. In Fig. 4(a) the normalized partial widths are given as a function of asymmetry for a few values of n, in Fig. 4(b), they are given as a function of n for a few asymmetries. At values close to symmetry, the lowest mode dominates, but, with increasing asymmetry, the higher n modes play an ever increasing role. The widths are zero when a half-multiple of the wavelength for a mode matches the value of b. In Fig. 5 the width arising from the first n modes is given for a few n values as a function of Q. This shows that an experimentally observed width, especially in asymmetric systems may include the comparable contribution of several modes.

It is clear that any attempt to relate such width to a single E1 mode rather than to the combination of several isovector modes may be doomed to failure. The difficulties are compounded by the use of a stiffness constant which may dramatically depend on the form of the standing wave, and which has been calculated incorrectly so far, even for the lowest mode. The cylindrical geometry is likely to be a poor approximation, but the introduction of a neck to better simulate the separation of the fragments leads to complications which may involve non-linear and dispersive effects. Dynamics is especially important, since the salient feature of this problem is the configuration associated with the neck snapping.

In conclusion, information on the isovector modes from the measurement of the charge fluctuation at high temperatures can only be obtained by properly accounting for both the effect of mass asymmetry and the role of higher order modes.

3. ANGULAR MOMENTUM TRANSFER

3.1 General features

The interactions between two colliding nuclei, especially those associated with short range forces, both conservative and dissipative, create strong torques responsible for transfer of angular momentum from orbital motion to intrinsic rotation of the fragments. The magnitude of the transferred angular momentum can be determined in various ways. The measurement of the γ-ray multiplicity is one such method of quite general application. By this technique, the angular momentum transfer has been studies as a function of Q value and of exit-channel mass asymmetry.

The general rise of the multiplicity with increasingly negative Q values (Fig. 6) is attributed mainly to the progressive tendency towards the rigid rotation limit expected as the Q value and the interaction times increase.[6] The V shaped dependence of the γ-ray multiplicity upon mass asymmetry (Fig. 7) in the quasi elastic region[7] is interpreted as a general tendency to transfer angular momentum with transferred mass on one hand, and as due to an increased Q value observed with increased net mass transfer on the other. Of course if energy is transferred only through mass exchange, the two explanations are identical.

In the deep-inelastic region, two extreme cases have been observed. In the first case, when a narrow l-window is available for deep inelastic products, a multiplicity rising with increasing asymmetry is observed[8,9] in agreement with the rigid rotation limit, as shown in Fig. 8. In the second case, when a very large l-window is available, the γ-ray multiplicity is essentially constant as a function of mass asymmetry. Examples of this case are readily available in the Kr-induced reactions[7] shown in Fig. 9. The accepted explanation of this behavior is an angular momentum fractionation along the mass asymmetry coordinate. Since large l-waves are associated with short lifetimes and vice-versa, small l-waves populate prevalently the large asymmetries, far removed from the entrance channel asymmetry. In this way the tendency of γ-ray multiplicities to increase with increasing asymmetry, as required by rigid rotation, is more or less compensated by the progressive decrease of the average angular momentum. All these effects are reasonably well understood on a more quantitative theoretical ground, as shown in Figs. 6 and 10 where the results of a diffusion model calculation are shown.[6]

3.2 Angular momentum Fractionation Along the Mass Asymmetry Coordinate in Compound Nucleus Fission and in Fusion-Fission

In the processes discussed above, the angular momentum fractionation appears to arise mainly from the decreasing rate of spread of the population along the mass asymmetry coordinate with increasing angular

momentum due to the dependence of the interaction time upon angular momentum.

Angular momentum fractionation is expected even when statistical equilibrium is attained along the ridge-line, either directly as the end product of diffusion, or through the population of the compound nucleus.[10] The reason for this can easily be seen. For sufficiently heavy systems the potential as a function of mass asymmetry (ridge potential[11]) has a minimum at symmetry whose second derivative increases with increasing angular momentum. At equilibrium, the mass distributions for large angular momenta are more sharply peaked about symmetry than the mass distributions for small angular momenta. It follows that, after summation over all partial l-waves, the angular momentum decreases with increasing asymmetry. This is a straightforward prediction that can be easily verified. More quantitatively, let us consider the ridge line as a function of mass asymmetry and angular momenta. For two touching liquid drop sheres of mass numbers A_1, A_2, the energy is:

$$E = \frac{2}{5} E_R \frac{1}{x(1-x)[x^{1/3} + (1-x)^{1/3}]^2 + \frac{2}{5}(x^{5/3} + (1-x)^{5/3})}$$

$$+ E_C\left\{\frac{5}{3}\frac{x(1-x)}{x^{1/3} + (1-x)^{1/3}} + x^{5/3} + (1-x)^{5/3}\right\} \qquad (12)$$

$$+ E_S\left\{x^{2/3} + (1-x)^{2/3}\right\}$$

where E_R, E_C, E_S are the rotational, Coulomb, and surface energies of the equivalent sphere, and $x = A_1/(A_1 + A_2)$.

Expanding about $x = 1/2$, we have:

$$E = (0.45354 + 1.29584\ y^2)E_R + (0.89244 + 0.46664\ y^2)E_C + (1.25992 - 0.55996\ y^2)E_S = \alpha E_R + \beta E_C + \gamma E_S \tag{13}$$

where $y = x - 1/2$.

Incidentally, it may be of interest to note the value of the fissionability parameter, $X = E_C/2E_S$, at which the second derivative at symmetry is zero (Businaro-Gallone point):

$$X_{BG} = \frac{3}{5} - 1.3885\ \frac{E_R}{E_S} \tag{14}$$

Now let us assume that a compound nucleus has been formed and that neutron decay and fission are the only competing processes. In the constant temperature limit, dropping l-independent factors and assuming $\Gamma_T \cong \Gamma_N$, we get

$$P(l,y) \quad \frac{\Gamma_F}{\Gamma_N}(l,y) \quad \propto \quad l e^{-(RE_R + CE_C + SE_S)/T}\ dl\ dy \tag{15}$$

where $R = \alpha - 1$, $C = \beta - 1$, $S = \gamma - 1$, and is the angular momentum. Integrating over angular momentum we obtain for a triangular distribution

$$P(y) \propto \frac{T}{\mathcal{R}E_R^{mx}} \left\{ \exp - \frac{CE_C + SE_S}{T} \right\} \left\{ \exp \left(\frac{\mathcal{R}E_R^{mx}}{T} \right) - 1 \right\} \qquad (16)$$

where E_R^{mx} is the maximum rotational energy of the equivalent sphere, and $\mathcal{R} = -R$. The last equation can be written in terms of the fissionability parameter X and the rotational parameter Y ($X = E_C/2E_S$, $Y = E_R/E_S$),

$$P(y) \propto \frac{1}{\mathcal{R}} \exp \left(- \frac{2E_S(CX + S/2)}{T} \right) \left\{ \exp \left(\frac{E_S}{T} \mathcal{R}Y_{mx} \right) - 1 \right\} \qquad (17)$$

The first moment of the angular momentum is:

$$\bar{l}(y) = l_{mx} \frac{\left[1 - \sqrt{\frac{T}{RE_R^{mx}}} F\left(\sqrt{\frac{\mathcal{R}E_R^{mx}}{T}} \right) \right] \exp \frac{\mathcal{R}E_R^{mx}}{T}}{\exp \frac{\mathcal{R}E_R^{mx}}{T} - 1} \qquad (18)$$

where

$$F(x) = e^{-x^2} \int_0^x e^{y^2} \, dy$$

is the Dawson integral and l_{mx} is the maximum of the entrance channel angular momentum distribution. The second moment of the angular momentum is:

$$\bar{l}^2(y) = l_{mx}^2 \frac{\left(1 - \frac{T}{\delta E_R^{mx}}\right)\exp \frac{\delta E_R^{mx}}{T} + \frac{T}{\delta E_R^{mx}}}{e^{\delta E_R^{mx}/T} - 1} \qquad (19)$$

One sees that the mass distributions for low values of l are considerably broader than those obtained for high l values. This is due to the fact that the minimum in the potential energy, which is shallow for the lower l values, becomes progressively deeper with increasing angular momentum, resulting in an increased concentration of the yield near symmetry. It is precisely this effect which leads to the fractionation of the angular momentum along the mass asymmetry coordinate. However, it is important to realize that the fissionability increases rapidly with l. This causes the distribution of angular momenta leading to fission to be narrower than the input triangular distribution and the overall average angular momentum leading to fission, $\bar{l}_D$, to be larger than that obtained by averaging over a triangular distribution. The resulting mass distribution, P(y), is narrow and resembles the mass distributions obtained for the highest l-values.

With these points in mind, the dependence of $\bar{l}$ and $\bar{l}^2$ as a function of y, is easily understood. For moderate values of y, both $\bar{l}/\bar{l}_D$ and $\bar{l}^2/\bar{l}_D^2$ are constant and close to unity. This is due to the fact that the high l-waves dominate the yield for this range of asymmetries, so that averaging over l yields a value of $\bar{l}$, $\bar{l}^2$ which is essentially $\bar{l}_D$, $\bar{l}_D^2$. However, the mass distributions for high l-waves are relatively narrow, and as one moves out to extreme asymmetries their contribution

to the total yield for a given asymmetry becomes less important, resulting in a slightly lower average ℓ.

The constant temperature approximation is fairly poor. In particular, it is rather unwise to drop the dependence of T on angular momentum. Furthermore, the approximation $\Gamma_f \ll \Gamma_n$ fails when the fission width is large. At the expense of an analytic answer, a more accurate picture can be obtained by including the angular momentum dependence of T and by replacing Γ_n with $\Gamma_n + \Gamma_f$. The results are shown in Figs. 11(a,b). One sees that the mass distributions for the high ℓ-waves are narrower because of the lower temperature. On the other hand, the ℓ-integrated mass distribution is somewhat broader because of the diminished weight given to the high ℓ-waves by the lower T and the division by Γ_T. These refinements cause $\bar{\ell}$, $\overline{\ell^2}$ to drop off more as one moves to larger asymmetries (see Fig. 11(b)). However, the qualitative interpretation is similar to that described above: $\bar{\ell}$, $\overline{\ell^2}$ are nearly constant as a function of y for small y due to the dominance of the high ℓ-waves, and then drop off rather abruptly because of the small contribution of the high ℓ-waves to the extreme asymmetries.

Another case which may be relevant in heavy-ion reactions arises when the system equilibrates along the ridge line and decays without passing through the compound nucleus stage. In other words, there is no competition from neutron emission or from other particle decay modes. In this case, Eqs. (15,16,18,19) must be modified as follows:

$$P(\ell,y) = A(\ell,T)\ \ell e^{-(RE_R + CE_C + SE_S)/T}\, d\ell\, dy \qquad (20)$$

where

$$A(l,T) = \left(\int e^{-(RE_R + CE_C + SE_S)/T_{dy}}\right)^{-1} .$$

Then

$$P(y) = \int P(l,y)\, dl \tag{21}$$

and

$$\bar{l}(y) = \int lP(l,y)dl/P(y) \tag{22}$$

$$\overline{l^2}(y) = \int l^2\, P(l,y)dl/P(y) \tag{23}$$

Notice that the difference between Eq. (15) and Eq. (20) resides only in the factor A(l,T) which is absent in the former case and present in the latter. Calculations based upon this second set of equations are shown in Fig. 12(a,b). The mass distributions for the individual l-waves shown in Fig. 12(a) are identical to those in Fig. 11(a) since the effect of neutron competition only changes the normalization (the mass distributions in the plots have all been normalized to unity to facilitate comparison). However, the distribution P(y) is now considerably broader than its counterpart in Fig. 11(a) due to the change in the weighting of P(l,y) in the integration over l.

The most significant effect of the assumption of equilibration along the ridge line can be seen in Fig. 12(b). In constrast to the preceding case (neutron competition), where $\bar{l}$ and $\overline{l^2}$ remained constant out to

moderate asymmetries and then dropped off rapidly, $\bar{l}$ and $\overline{l^2}$ peak at symmetry and fall off more gradually with increasing y, giving rise to curves which are gaussian in appearance. The dramatic differences in the l-fractionation imply that it may be possible to distinguish between the two mechanisms, i.e. compound nucleus fission and non-compound nucleus decay, by measuring the angular momentum as a function of asymmetry. This result is particularly important in light of the fact that there are a number of examples[12-15] in heavy ion reactions where fission-like mass distributions occur which are difficult to explain in terms of compound nucleus decay.

4. ANGULAR MOMENTUM FLUCTUATIONS

4.1 The Second Moments of the γ-Ray Multiplicities and Their Sources

Recent measurements of the 2nd moments of the γ-ray multiplicities[16] indicate that they are substantially larger than the values expected from a 2I + 1 distribution ($\sigma/I = 0.35$). When the measurements are performed as a function of Z, the diffusion process which, as was mentioned above, can fractionate the angular momentum, can also introduce a substantial second moment as can be seen from this simple exercise.

Let us use an analytic diffusion model without drift to interpret the dependence of the angular momentum distributions upon mass asymmetry.[17] The solution of the Fokker-Planck equation takes the form

$$P(Z,t) = [4\pi\mu_2 t]^{-1/2} \exp - (Z - Z_p)^2/2\mu_2 t \qquad (24)$$

where P is the probability of producing a complex with asymmetry Z after an interaction time t, Z_p is the entrance channel asymmetry, and μ_2 is the spread coefficient. The cross section for a given impact parameter b can be expressed as:

$$\Phi(Z,b) = N[\tau(b)]^{-1/2} b \exp[-(Z - Z_p)^2/2\mu_2 \tau(b)]. \quad (25)$$

A simple form for the interaction time $\tau(b)$ is: $\tau(b) = \tau_0(1 - b/b_{max})$. By defining $\beta = (Z - Z_p)^2/2\mu_2\tau_0$, and by changing variables to $\eta = b/b_{max}$, one arrives at the distribution function

$$\Phi(\beta,\eta) = N[1 - \eta]^{-1/2} \beta^{-1/2} \eta \exp[-\beta/(1 - \eta)]. \quad (26)$$

Given the angular momentum limits η_1, η_2 and the asymmetry β, one may write the moments of the angular momentum distribution as

$$\mu_m = \int_{\eta_1}^{\eta_2} \eta^m \Phi(\beta,\eta) d\eta = \int_{\eta_2}^{\eta_1} \frac{\eta^{m+1}}{[1 - \eta]^{1/2}} \exp -\beta/(1 - \eta) d\eta \quad (27)$$

By making the change of variable $x = (1 - \eta)^{-1}$ and defining $u_i = (1 - \eta_i)^{-1}$ for i = 1,2, one arrives at

$$\mu_m = \sum_{i=0}^{m+1} (-i)^i \binom{m+1}{i} \xi_i(u_1,u_2,\beta) \quad (28)$$

where

$$\xi_i(u_1,u_2,\beta) = \int_{u_1}^{u_2} x^{-(i+3/2)} e^{-\beta x} dx . \quad (29)$$

The integrals ξ_i satisfy a recurrence relation

$$\xi_i = \frac{1}{i + 1/2}\left[\frac{e^{-u_i}}{u_1^{i+1/2}} - \frac{e^{-u_2}}{u_2^{i+1/2}} - \beta\xi_{i-1}\right] \quad . \qquad (30)$$

In order to evaluate the desired integrals, it is sufficient to evaluate one of them separately. Application of the recurrence relation now allows evaluation of all desired ξ_i's, and thus all necessary μ_m's.

Consider a system in which essentially all impact parameters contribute to the deep inelastic process. In order to leave out events in which the kinetic energy in incompletely damped, it is assume that $\eta_1 = 0$ and $\eta_2 = 0.9$, thus allowing 20 percent of the cross section for incompletely damped (QE) events. Three very striking features, shown in Fig. 13, emerge: (1) The mean angular momentum $\langle \eta \rangle$ decreases as a function of β. (2) The ratio $\rho = \sigma/\langle \eta \rangle$ exceeds the 2 I+ 1 value for nearly all asymmetries. (3) The skewness γ changes sign as a function of asymmetry.

In order to compare with experiment, it is necessary to correlated β with Z. From previous work in fitting data from 620 Mev ^{86}Kr + ^{197}Au, the following parameters are used: $\mu_2 = 6.6 \times 10^{21}\ e^2 sec^{-1}$, $\tau_0 = 4.0 \times 10^{-21}$ sec. To calculate the γ-ray multiplicity, $M_\gamma(Z)$, we assume rigid rotation. Then one has $M_\gamma(Z)/1/2|_{max} = f(Z)\langle \eta(\beta)\rangle$, where f(Z) is the fraction of the angular momentum tied up in the fragment spins. The curve of asterisks in Fig. 13 is a plot of this quantity. As can be

seen, the multiplicities are approximately constant as a function of Z, in agreement with the data. Large values of γ are predicted in excess of those expected from a $2I + 1$ distribution.

A much better indicator of spin fluctuations is the degree to which the fragment spins are misaligned. This misalignment, as we shall see, can be readily detected by measuring the angular distributions of γ-rays, α particles, fission fragments emitted from the primary deep inelastic fragments. The origin of these fluctuations can be quantal or classical, and can be due either to non equilibrium or equilibrium processes. Let us consider first one example of equilibrium quantal fluctuations and examples of thermal fluctuations later on.

4.2 Quantal Effects

In view of the analogy between spin and isospin we can take advantage of the cylinder model results obtained in Section 2.

Instead of neutron and proton fluids, we consider now two new nucleon fluids, one with positive and the other with negative spin projection on the cylinder axis.

Let us assume that the density of the doubly degenerate single particle levels is g and that the average spin projection of each particle on the cylinder axis is M. Then n aligned broken pairs will generate an angular momentum:

$$I = 2nM \tag{31}$$

and an energy:

$$U = \frac{n^2}{g} \tag{32}$$

which leads to the relation:

$$U = \frac{I^2}{4M^2 g} = \frac{I^2}{2\mathcal{I}} \tag{33}$$

where $\mathcal{I} = 2M^2 g$ is the moment of inertia of the cylinder.

In analogy with the symmetry energy we can write the rotational energy U as:

$$U = x_I \frac{I^2}{A} \quad \text{with} \quad x_I = \frac{A}{2\mathcal{I}} \tag{34}$$

Now a perturbation consisting in a variation of the angular velocities of contiguous perpendicular slices of the cylinder will move with a velocity (spin velocity):

$$u^2 = 8x_I \frac{\rho_0^+ \rho_0^-}{m\rho_0^2} = 2\frac{x_I}{m} \tag{35}$$

where ρ_0^+, ρ_0^-, ρ_0 are the equilibrium densities of right-handed, left-handed and total fluid, and m is the nucleon mass.

The eigen-modes are defined as in the case of isospin. Their quantization leads to the phonon energies:

$$\hbar\omega_n = \frac{\hbar u \pi}{2a} n \tag{36}$$

a being the half-length of the cylinder and n the order of the mode.

The stiffness constants are:

$$c_n = \frac{4\pi^2 \chi_I}{A} \frac{n^2}{\sin^2[n\pi Q]} \tag{37}$$

Q being the asymmetry of the cut as in the previous section.

The widths are:

$$\sigma_n^2 = \sigma_1^2(\text{symmetry}) \frac{\sin^2[n\pi Q]}{n} \tag{38}$$

where

$$\sigma_1^2(\text{symmetry}) = \frac{\hbar\omega_1}{c_1} = \frac{\hbar}{8\pi a} \sqrt{\frac{A\mathcal{J}}{m}} \tag{39}$$

For a cylinder approximating two equal touching spheres and for A = 200 the width of the lowest mode is

$$\sigma_1(\text{symmetry}) = 1.7\ \hbar$$

As we shall see this quantal width is negligible as compared to that expected from thermal fluctuations.

4.3 Statistical Excitation of Angular Momentum Bearing Modes

Let us consider a frame of references where the z axis is parallel to the entrance-channel angular momentum, the x axis parallel to the recoil direction of one of the fragments, and the y axis perpendicular to the z,x plane.

A misalignment of the fragment angular momentum arises when non-vanishing x and y components of the fragment angular momentum are present. Among the possible sources of these components, the thermal excitation of angular momentum-bearing modes of the intermediate complex appears very likely and can be readily investigated.[10]

4.4 Statistical Coupling Between Orbital and Intrinsic Angular Momenta and Wriggling Modes

Let us assume that we can approximate the exit channel configuration by two touching, equal, rigid spheres with all the associated rotational degrees of freedom. As we shall see, this model leads to simple analytical predictions for the relevant statistical distributions.

First, let us consider the equilibrium between intrinsic rotation of the fragments and their orbital rotation, assuming that the relevant angular momenta are all parallel to each other. If the total angular momentum is I and the spin fragment is s, the energy for an arbitrary partition between orbital and intrinsic angular momentum is:

$$E(s) = \frac{(I - 2s)^2}{2\mu r^2} + \frac{2s^2}{2\mathcal{I}} = \left(\frac{2}{\mu r^2} + \frac{1}{\mathcal{I}}\right)s^2 - \frac{2I}{\mu r^2}\, s + \frac{I^2}{2\mu r^2} \tag{40}$$

The first term is the orbital and the second the intrinsic rotational energy, $\mathcal{I}$ being the moment of inertia of one of the two equal spheres.

The partition function is given by:

$$Z \propto e^{-E(s)/T}ds = \sqrt{\frac{\pi\mu r^2 \mathcal{I} T}{2\mathcal{I} + \mu r^2}}\ \exp\left\{-\frac{I^2}{2T(2\mathcal{I} + \mu r^2)}\right\}. \tag{41}$$

The average spin for both fragements is given by

$$2\bar{s} = \frac{2\int s\, e^{-E(s)/T}ds}{Z} = \frac{2\mathcal{I}}{\mu r^2 + 2\mathcal{I}}\, I = \frac{2}{7}\, I = 2I_R. \tag{42}$$

The second moment $\overline{s^2}$ is given by

$$4\overline{s^2} = \frac{2\mu r^2 \mathcal{I} T}{(\mu r^2 + 2\mathcal{I})} + \frac{4\, I^2 \mathcal{I}^2}{(\mu r^2 + 2\mathcal{I})^2}\ . \tag{43}$$

From this we obtain the standard deviation

$$4\sigma_s^2 = \frac{2\mathcal{I}\mu r^2 T}{(\mu r^2 + 2\mathcal{I})} = \frac{10}{7}\mathcal{I}T. \tag{44}$$

The result in (42) is temperature independent as one should have expected from the fact that (40) is quadratic in s. It could in fact be obtained by solving the equation

$$\frac{dE}{ds} = 0. \tag{45}$$

This result corresponds to the mechanical limit of rigid rotation when the orbital and the intrinsic angular velocities are matched.

The result in (44) could have been obtained also by appreciating that the thermal fluctuations about the average in (42) are controlled by the second derivative of (40) at the minimum, or:

$$4\sigma_s^2 = 4T/b, \tag{46}$$

where

$$b = \left.\frac{\partial^2 E}{\partial s^2}\right|_{\bar{s}} .$$

It is important to appreciate the meaning of (44). The quantity $4\sigma^2$ represents the amount of angular momentum trade-off allowed by the temperature, between orbital and intrinsic rotation. It should correspond exactly to the long time limit of σ_z^2 of Ayik et al.[18] Just because of the meaning of this trade-off, it is unwarranted to assume a priori that similar values should be taken by σ_x^2 and σ_y^2, however defined (other orthogonal rotational modes), as implied in the same paper.

In some instances, such as γ-multiplicity measurements, one is interested in the average sum of the moduli of the fragment spins. This can be obtained from

$$2|\bar{s}| = \int |s|\, e^{-E(s)/T}\, ds/Z \ ,$$

which yields

$$2|\bar{s}| = 2\left[\left(\frac{\mu r^2 \mathcal{I} T}{\pi(\mu r^2 + 2\mathcal{I})}\right)^{1/2} \exp\left(-\frac{\mathcal{I} I^2}{\mu r^2 T(\mu r^2 + 2\mathcal{I})}\right) + I\,\frac{\mathcal{I}}{(\mu r^2 + 2\mathcal{I})}\ \mathrm{erf}\left\{I\left(\frac{\mathcal{I}}{(\mu r^2 T(\mu r^2 + 2\mathcal{I})}\right)^{1/2}\right\}\right] \ , \tag{47}$$

or, in dimensionless form,

$$\frac{2|\bar{s}|}{\sqrt{\mathcal{I}^* T}} = 2\left[\frac{1}{\sqrt{\pi}} \exp(-x^2) + x\ \mathrm{erf}(x)\right] \ , \tag{48}$$

where $x = I_R/\sqrt{\mathcal{I}^* T}$ and $\mathcal{I}^* = \mu r^2/(\mu r^2 + 2\mathcal{I})$. Also $I_R = I/7$ is the spin per fragment arising from rigid rotation. The above expression is plotted in Fig. 4. In the limit of large I, one recovers (42):

$$2|\bar{s}| = \frac{2\mathcal{I} I}{\mu r^2 + 2\mathcal{I}} = \frac{2}{7} I \ .$$

For small I,

$$\frac{2|\bar{s}|}{\sqrt{\mathcal{I}^* T}} = \frac{2}{\sqrt{\pi}}(1 + x^2) \ ,$$

to order x^2, so for I = 0 one obtains

$$2|\overline{s}| = 2\sqrt{\frac{4T}{\pi}}\left(\frac{\mu r^2}{\mu r^2 + 2\mathcal{I}}\right)^{1/2} = 2\sqrt{\frac{5\mathcal{I}T}{7\pi}} \quad . \tag{49}$$

The second moment, still given by Eq. (43) can be rewritten as: $\overline{4s^2} = 2\mathcal{I}^*T + 4I_R^2$. In this case the fragment angular momentum at zero angular momentum arises from the excitation of a collective mode (wriggling[19]) in which the two fragments spin in the same direction while the system as a whole rotates in the opposite direction in order to maintain I = 0. Contrary to what has been assumed thus far, the wriggling mode is actually doubly degenerate, as illustrated in Fig. 15. Considering first the two-fold degenerancy of the wriggling mode in the limit, I = 0, one obtains:

$$E(s) = \frac{s^2}{\mathcal{I}} + \frac{4s^2}{2\mu r^2} = \left(\frac{1}{\mathcal{I}} + \frac{2}{\mu r^2}\right) s^2 = \frac{s^2}{\mathcal{I}^*} \quad , \tag{50}$$

$$Z \propto \mathcal{I}^*T \quad , \tag{51}$$

$$2|\overline{s}| = \sqrt{\pi \mathcal{I}^*T} \tag{52}$$

$$\overline{4s^2} = 4\mathcal{I}^*T \tag{53}$$

and

$$\sigma^2 = (4 - \pi)\mathcal{I}^*T \quad . \tag{54}$$

Let us now couple this doubly degenerate mode to the spin arising from rigid rotation. If the aligned component of the angular momentum arising from rigid rotation is I_R and that due to wriggling is R, the total angular momentum for each fragment is

$$s^2 = I_R^2 + R^2 + 2I_R R \cos\theta \tag{55}$$

The orbital angular momentum is

$$\begin{aligned} I_T^2 &= I^2 + 4R^2 - 4IR\cos\theta \\ &= (I - 2I_R)^2 + 4R^2 - 4(I - 2I_R)R\cos\theta \end{aligned} \tag{56}$$

and the total energy is

$$E = \frac{35I_R^2 + 14R^2}{10.4} \tag{57}$$

The partition function

$$Z \propto \iint R \exp(-E/T)dRd\theta$$

is readily evaluated and yields

$$\ln Z = \ln \frac{4T}{1.4} - \frac{3.5\ I_R^2}{4T} + \text{const.} \tag{58}$$

The angular momentum of either fragment is

$$s = \sqrt{I_R^2 + R^2 + 2I_R R \cos\theta} \quad ,$$

so the average sum of the moduli of the fragment spins is

$$2\overline{|s|} = \frac{2}{Z}\iint \sqrt{I_R^2 + R^2 + 2I_R R \cos\theta}\; R \exp(-E/T)\,dR\,d\theta \quad . \qquad (59)$$

The double integral in Eq. (59) cannot be evaluated in closed form. However, for large I_R and small I_R one can immediately obtain the integral over θ:

$$\begin{cases} 2I_R + \dfrac{R^2}{2I_R} & \text{for } I_R \gg R \\ 2R + \dfrac{I_R^2}{2R} & \text{for } I_R \ll R \end{cases} \quad .$$

The above are only limiting expressions, but they can be used as interpolation formulae from 0 to I_R and from I_R to ∞. Taken together the expressions above form a continuous function at $R = I_R$. The integral, moreover, is a continuous function along with its first derivative on the interval $(0,\infty)$ and yields a rather accurate approximation to $2\overline{|s|}$. It is given by:

$$2\overline{|s|} = 2I_R + \frac{\mathcal{J}^*T}{2I_R} - \frac{1}{2}\left(I_R + \frac{\mathcal{J}^*T}{I_R}\right)\exp\left(-\frac{I_R^2}{\mathcal{J}^*T}\right) + \sqrt{\pi}\left(\sqrt{\mathcal{J}^*T} + \frac{I_R^2}{2\sqrt{\mathcal{J}^*T}}\right)\operatorname{erfc}\left(\frac{I_R}{\sqrt{\mathcal{J}^*T}}\right) \quad , \qquad (60)$$

where again $\mu^* = \mu r^2 \omega / (\mu r^2 + 2\mathcal{I}) = \omega/1.4$. In dimensionless form:

$$\frac{2\overline{|s|}}{\omega^* T} = 2x + \frac{1}{2x} - \frac{1}{2}\left(x + \frac{1}{x}\right)\exp(-x^2) + \sqrt{\pi}\left(1 + \frac{x^2}{2}\right)\operatorname{erfc}(x) \qquad (61)$$

This function, which is plotted in Fig. 14, has the following limiting values:

$$\frac{2\overline{|s|}}{\omega^* T} = \sqrt{\pi}\left(1 + \frac{x^2}{2}\right) \quad , \text{ small } I_R \qquad (61a)$$

$$\frac{2\overline{|s|}}{\omega^* T} = 2x + \frac{1}{2x} \quad , \text{ large } I_R \qquad (61b)$$

Also in the limit of large I_R, one obtains

$$4\sigma^2 = 4I_R^2 + 4\overline{R^2} - 4I_R^2 - 2\overline{R^2} = 2\overline{R^2} = 2\omega^* T \qquad (62)$$

where $\overline{R^2} = \omega^* T$.

It is interesting to note that the wriggling mode generates a random angular momentum in a plane perpendicular to the line of centers of the fragments. The vector sum of this random angular momentum and that arising from rigid rotation thus leads to a fluctuation in the orientation of the total spin, again in the plane perpendicular to the separation axis. The corresponding rms angle is easily obtained from

$$\tan\theta = \sqrt{\frac{\overline{R^2}}{I_R^2}} = \sqrt{\frac{\omega^* T}{I_R^2}} = \sqrt{\frac{5\omega T}{7I_R^2}} \qquad (63)$$

4.5 Thermal Fluctuation of the Angular Momentum Projection on the Disintegration Axis: Tilting

Above, we have assumed that the two touching fragments are aligned with their common axis perpendicular to the total angular momentum. Because of the thermal fluctuations, this condition can be relaxed (see Fig. 15). Assuming now that the two fragments are rigidly attached one to the other, the energy is given by

$$E = \frac{I^2 - K^2}{2\mathcal{J}_\perp} + \frac{K^2}{2\mathcal{J}_\parallel} = \frac{I^2}{2\mathcal{J}_\perp} + \frac{K^2}{2\mathcal{J}_{eff}} \tag{64}$$

where: $\mathcal{J}_\perp = 2\mathcal{J} + \mu r^2$; $\mathcal{J}_\parallel = 2\mathcal{J}$; and $\mathcal{J}_{eff}^{-1} = \mathcal{J}_\parallel^{-1} - \mathcal{J}_\perp^{-1}$; K is the projection of the angular momentum I along the line of centers. The partition function is:

$$Z = \sqrt{\pi}\, \exp(-I^2/2\mathcal{J}_\perp T)\, \sqrt{2\mathcal{J}_{eff}T}\, \mathrm{erf}(I/\sqrt{2\mathcal{J}_{eff}T}) \tag{65}$$

from which

$$\overline{K^2} = \mathcal{J}_{eff}T - \frac{I\sqrt{2\mathcal{J}_{eff}T}}{\sqrt{\pi}}\, \frac{\exp - I^2/2\mathcal{J}_{eff}T}{\mathrm{erf}\ I/\sqrt{2\mathcal{J}_{eff}T}} \tag{66}$$

For small I we have

$$\overline{K^2} = \frac{1}{3} I^2 \tag{67a}$$

while for large I we have:

$$\overline{K^2} = \mathcal{J}_{eff} T = \frac{14}{5} \mathcal{J} T \tag{67b}$$

The total fragment spin is given by

$$2s = \sqrt{K^2 + \frac{4}{49}(I^2 - K^2)} \tag{68}$$

and the averaged square quantity is

$$4\overline{s^2} = \overline{K^2} + \frac{4}{49} I^2 - \frac{4}{49} \overline{K^2} = \frac{45}{49} \overline{K^2} + \frac{4}{49} I^2 \tag{69a}$$

and for large I,

$$4\overline{s^2} = \frac{18}{7} \mathcal{J} T + \frac{4}{49} I^2 \tag{69b}$$

The average, on the other hand, is

$$2\bar{s} = \frac{\int \frac{2}{7} I \left(1 + \frac{45}{4} \frac{K^2}{I^2}\right)^{1/2} e^{-E/T} dK}{Z} \simeq \frac{2}{7} I + \frac{\int \frac{45}{28} \frac{K^2}{I} e^{-E/T} dK}{Z}$$
$$= \frac{2}{7} I + \frac{45}{28} \frac{\overline{K^2}}{I} = \frac{2}{7} I \left(1 + \frac{45}{8} \frac{\overline{K^2}}{I^2}\right) = 2I_R + \frac{9}{14} \frac{\mathcal{J} T}{I_R} \tag{70}$$

where we have dropped terms of order higher than K^2/I^2. From the above equations one learns that the total angular momentum of the fragments is only slightly affected by the thermal fluctuations of the separation axis and that the correction to the ordinary rigid rotation

limit, at constant temperature, decreases as I^{-1}. Furthermore, the fluctuation $\sigma^2 \approx 0$ up to order $\overline{K^2}/I^2$ and can be neglected in most cases.

Due to the excitation of this mode the reaction plane is not perpendicular to the total angular momentum of the system I, but is "tilted" by an angle θ_t given by

$$\sin\theta_t = \sqrt{\frac{\overline{K^2}}{I^2}} \tag{71}$$

The angle more relevant to sequential fission angular distributions is the angle between the total spin of one fragment and the normal to the line of centers (in the same plane as I), which is given by

$$\sin\theta = \sqrt{\frac{\overline{K^2}}{4\overline{s^2}}} \tag{72}$$

Since I may be considerably larger than s, this angle can be considerably larger than θ_t. One should note that the combined effect of wriggling and tilting will produce spin components along all the coordinate axes. If the separation axis is the z-axis, tilting will lead to an rms z-component of $\sqrt{\overline{K^2}/4} = 0.84\sqrt{\mathcal{I}T}$ for each fragment. On the other hand, the rms x- and y-components due to wriggling will be $\sqrt{\overline{R^2}/2} = 0.60\sqrt{\mathcal{I}T}$; hence, tilting and wriggling together generate an angular momentum which is randomly and almost isotropically distributed in three dimensions.

4.6 Twisting and Bending Modes Excited in a Zero Angular Momentum System

These three degrees of freedom are illustrated in Fig. 16. They are degenerate in our two-equal-sphere model. A splitting of the degeneracy could easily occur in the case of fragment deformation. We shall not consider this rather important possibility at the moment, although it is completely trivial, because of the arbitrariness in the choice of deformation.

The partition function can be written as:

$$Z = \int R^2 \exp(-R^2/\lambda T)dR \tag{73}$$

and

$$\ln Z = A - \frac{3}{2} \ln \frac{1}{\lambda T} \tag{74}$$

from which

$$\overline{R} = \frac{2}{\sqrt{\pi}}(\lambda T)^{1/2} \quad , \tag{75}$$

$$\overline{R^2} = -\frac{\partial \ln Z}{\partial[1/\lambda T]} = \frac{3}{2}\lambda T \tag{76}$$

and

$$\sigma_R^2 = \left(\frac{3}{2} - \frac{4}{\pi}\right)\lambda T \cong 0.227\lambda T \quad . \tag{77}$$

Notice that R is the angular momentum of <u>each</u> fragment and that, for each mode, the angular momenta of the two fragments cancel out pairwise. Furthermore, for each fragment the resulting angular momentum is randomly oriented. It is worth stressing again that this angular momentum can exist even when the total angular momentum is zero because of the pairwise cancellation mentioned above.

4.7 Coupling of Twisting and Bending Modes to Rigid Rotation

We want to generalize the previous calculation to the case of nonzero total angular momentum. Let us assume that <u>each</u> fragment has an aligned angular momentum component I_R arising from rigid rotation and a random component R due to the bending and twisting modes. The overall rotational energy arising from the fragment spins is:

$$E = \frac{1}{2\mathcal{J}}\left\{(I_R^2 + R^2 + 2RI_R\cos\theta) + (I_R^2 + R^2 - 2RI_R\cos\theta)\right\} = \frac{1}{\mathcal{J}}(I_R^2 + R^2) \quad (78)$$

The average total angular momentum of the fragments is:

(79)

$$2|\bar{S}| = \frac{2\pi\iint\left(\sqrt{I_R^2 + R^2 + 2I_R\cos\theta} + \sqrt{I_R^2 + R^2 - 2I_R R\cos\theta}\right)R^2\exp\left(-\frac{R^2}{\mathcal{J}T}\right)dR\sin\theta\,d\theta}{2\pi\iint R^2\exp\left(-\frac{R^2}{\mathcal{J}T}\,dR\right)\sin\theta\,d\theta}$$

The integral over θ yields

$$2I_R + \frac{2}{3}\frac{R^2}{I_R} \qquad \text{for} \quad I_R > R$$

$$2R + \frac{2}{3}\frac{I_R^2}{R} \qquad \text{for} \quad I_R < R \quad .$$

Thus caution is necessary in calculating the thermal average. The result is

$$2\overline{|s|} = \left(2I_R + \frac{\frac{1}{3}T}{I_R}\right) \mathrm{erf}(I_R/\sqrt{\tfrac{1}{3}T}) + \frac{2}{\sqrt{\pi}}\sqrt{\tfrac{1}{3}T}\exp(-I_R^2/\tfrac{1}{3}T). \qquad (80)$$

This expression can be written in dimensionless form as

$$\frac{2\overline{|s|}}{\sqrt{\frac{1}{3}T}} = \left(2x + \frac{1}{x}\right)\mathrm{erf}(x) + \frac{2}{\sqrt{\pi}}\exp(-x^2) \quad , \qquad (81)$$

where $x = I_R/\sqrt{\frac{1}{3}T}$. This function is plotted in Fig. 17. For small x one obtains

$$\frac{2\overline{|s|}}{\sqrt{\frac{1}{3}T}} \cong \frac{4}{\sqrt{\pi}}\left(1 + \frac{x^2}{3}\right) \qquad (82)$$

In the limit of $I_R = 0$, one obtains

$$2\overline{|s|} = \frac{4}{\sqrt{\pi}}\sqrt{\tfrac{1}{3}T} = 2\overline{R} \qquad (83)$$

in agreement with the results of the last section. For large x,

$$\frac{2\overline{|s|}}{\sqrt{\Delta T}} = 2x + \frac{1}{x} \tag{84}$$

or

$$2\overline{|s|} = 2I_R + \frac{\Delta T}{I_R} = 2I_R + \frac{2}{3}\frac{\overline{R^2}}{I_R} = \frac{2}{7} I \left(1 + \frac{49}{2}\frac{\Delta T}{I^2}\right) \tag{85}$$

Similarly the average square angular momentum is

$$4\overline{s^2} = 2I_R^2 + 2\overline{R^2} + 2\int \left\{\frac{1}{2}\sqrt{I_R^4 + R^4 - 2I_R^2R^2} + \frac{(I_R^2 + R^2)^2}{4RI_R} \sin^{-1}\frac{2I_R R}{I_R^2 + R^2}\right\} R^2 \tag{86}$$

$$\times \exp\left(-\frac{R^2}{\Delta T}\right) dR \ ,$$

which, to order $\overline{R^2}/I_R^2$, yields

$$4\overline{s^2} = 4(I_R^2 + \overline{R^2}) \tag{87}$$

$$4\sigma^2 = \frac{4}{3}\overline{R^2} = 2\Delta T \ . \tag{88}$$

In this case as well as in Eqs. (70) and (61b) we see that the correction to the rigid rotation limit decreases as I^{-1} in Eq. (85), but with a slightly larger coefficient. However, there is some appreciable contribution to the width. Of greatest importance is the fact that a sizeable "tilt" of the angular momentum of each fragment about the direction of the total angular momentum is introduced

$$\tan\theta \cong \sqrt{\frac{\overline{R^2}}{I_R^2}} = \sqrt{\frac{3\hbar^2 T}{2I_R^2}} \tag{89}$$

This depolarization is of great importance for the proper interpretation of the out-of-plane angular distribution of gamma rays emitted by the fragments and of the out-of-plane angular distribution of sequential fission fragments.[20] Note that the effect on the depolarization in Eq. (89) is larger than that due to the combination of tilting and wriggling.

4.8. A Simple Application to a Typical Heavy-Ion Reaction

It should be stressed again that the above formalism applies strictly to a system which has reached statistical equilibrium. In general this is not the case in heavy-ion reactions, especially insofar as the mass asymmetry degree of freedom is concerned. However, for other degrees of freedom statistical equilibrium may be reached or closely approached. At any rate, it is interesting to compare the predictions of an equilibrium model with experiment.

The reaction which we want to consider is 600 MeV ^{86}Kr + ^{197}Au.[20] Some of the vital statistics of this reaction are summarized in Table 1. If we allow the system to evolve to the configuration of two touching spheres ($r_0 = 1.22$) we have (either for l_{rms} or $\bar{l}$) an excitation energy of 113 MeV, so $T = 1.78$ MeV and $\sqrt{\mathcal{I}T} = 131\ \hbar^2$ or $\sqrt{\mathcal{I}T} \approx 12\ \hbar$.

Now let us first consider the effect of the doubly degenerate wriggling mode. For the average angular momentum the total spin is given by Eq. (61b),

$$2\overline{|s|} = \frac{2}{7}\,190 + \frac{7}{2}\,\frac{93.75}{190}$$

$$= 54.29 + 1.73 = 56.02\ \hbar$$

and from Eq. (62),

$$4\sigma^2 = 2(93.75) = 187.50\ \hbar^2 \ .$$

The fluctuation of the separation axis with respect to the total angular momentum yields the following from Eqs. (67b) and (70)

$$\overline{K^2} = \frac{14}{5}\,\overline{T} = 367.50\ \hbar^2$$

TABLE 1.

600 MeV ^{86}Kr + ^{197}au

E_{lab}	=	600 MeV
E_{cm}	=	418 MeV
B_{Coul}	=	283 MeV
E/B_{Coul}	=	1.48
l_{max}	=	285 $\hbar$
$l_{r.m.s}$		202 $\hbar$
$\overline{l}$	=	190 $\hbar$

$$2\bar{s} = \frac{2}{7}\,190 + \frac{9}{2}\,\frac{131.25}{190}$$

$$= 54.29 + 3.11 = 57.40\,\hbar \quad .$$

The out-of-plane tilting of the separation axis from Eq. (71) is

$$\theta = \sin^{-1}\left(\frac{\sqrt{367.50}}{190}\right) = 5.79^{\circ} \quad .$$

The depolarization of the fragment spin due to tilting can be estimated from Eq. (72)

$$\theta = \sin^{-1}\left(\frac{\frac{1}{2}\sqrt{367.50}}{28.70}\right) = 19.51^{\circ}$$

which is indeed substantial. The twisting and bending modes lead to

$$\overline{R^2} = \frac{3}{2}\,\mathcal{I}T = 196.88\,\hbar^2$$

$$2\bar{s} = \frac{2}{7}\,190 + 7\,\frac{131.25}{190}$$

$$= 54.29 + 4.84 = 59.13\,\hbar$$

$$4\sigma^2 = 2(131.25) = 262.50\,\hbar^2 \quad .$$

Let us now try to summarize the results on the fragment spin fluctuations. If one assumes a triangular distribution for the angular

momentum distribution (i.e., no l-fractionation), there is an additional contribution to the sigma squared of both fragments of

$$4\sigma^2 = \frac{4}{49}\left(\frac{l_{max}^2}{2} - \frac{4}{9}\, l_{max}^2\right) = 368.37\ \hbar^2 \ .$$

Summing all the fluctuations we obtain

$$4\sigma^2 = 818.37\ \hbar^2 \quad \text{or} \quad 2\sigma = 28.61\ \hbar \ .$$

In conclusion, without allowing for angular momentum fractionation, we obtain for the overall fragment spin

$$2\overline{|s|} \cong 64 \pm 29\ \hbar \ .$$

Thus we can see that the thermally excited normal modes contribute substantially to the spin fluctuations. Furthermore, the obtained fluctuation is comparable to that observed in Ref. 16.

Another interesting case is spin-generated by the wriggling, bending and twisting modes for zero total angular moment. For wriggling we obtain

$$2\overline{|s|} = \sqrt{\pi \mathcal{J}^* T} = 17.16\ \hbar \ .$$

Bending and twisting contribute

$$2s = \frac{4}{\sqrt{\pi}}\sqrt{\mathcal{J}T} = 25.85\ \hbar \ .$$

Combining both angular momenta one obtains

$$\sqrt{\overline{s^2}} = 15.5\ \hbar$$

for each fragment.

4.9 Overall angular momentum distribution function

In summary, the thermal excitation of the collective modes leads to Gaussian distributions in the three components I_x, I_y, I_z, namely:

$$P(\underset{\sim}{I}) \quad \exp - \left[\frac{I_x^2}{2\sigma_x^2} + \frac{I_y^2}{2\sigma_y^2} + \frac{(I_z - \bar{I}_z)^2}{2\sigma_z^2} \right] \tag{90}$$

where

$$\begin{aligned} \sigma_x^2 &= \sigma_{Tw}^2 + \sigma_{Ti}^2 = \frac{1}{2}\mathcal{I}T + \frac{7}{10}\mathcal{I}T = \frac{6}{5}\mathcal{I}T \\ \sigma_y^2 &= \sigma_B^2 + \sigma_w^2 = \frac{1}{2}\mathcal{I}T + \frac{5}{14}\mathcal{I}T = \frac{6}{7}\mathcal{I}T \\ \sigma_z^2 &= \sigma_B^2 + \sigma_w^2 = \frac{1}{2}\mathcal{I}T + \frac{5}{14}\mathcal{I}T = \frac{6}{7}\mathcal{I}T \quad . \end{aligned} \tag{91}$$

where the subscripts stand for Twisting (Tw), Tilting (Ti), Bending (B), Wriggling (W). The quantity $\mathcal{I}$ is the moment of inertia of one of the two touching spheres, and T is the temperature.

The assumption of two equal touching spheres is admittedly schematic. However, the generalization to two equal touching spheroids is completely trivial and left to the readers who may have a better idea about the fragment deformation at the scission configuration.

5. ANGULAR DISTRIBUTIONS

5.1. Angular Distributions of Sequential Fission and of Sequential Light Particle Emission

The magnitude of the angular momentum misalignment can be measured through the in- and out-of-plane angular distribution of the decay products of one of the two fragments.[21] We have shown elsewhere[11] that the angular distribution of fission fragments and of light particles emitted by a compound nucleus can be treated within a single framework.

The direction of emission of a decay product (fission fragment, α-particle, etc) is defined by the projection K of the fragment angular momentum on the disintegration axis. Simple statistical mechanical considerations show that the distribution in K values is Gaussian.

Specifically for any given K the particle decay width can be written as:

$$\Gamma_K^I \, dK = \Gamma^\circ \exp\left[-\frac{\hbar^2 I^2}{2T}\left(\frac{1}{\mathcal{J}_\perp} - \frac{1}{\mathcal{J}_c}\right)\right] \exp\left(-\frac{K^2}{2K_o^2}\right)\frac{dK}{I} \qquad (92)$$

where Γ° is an angular momentum independent quantity; T is the temperature; $K_o^2 = \hbar^{-2}(1/\mathcal{J}_\parallel - 1/\mathcal{J}_\perp)^{-1}T$; $\mathcal{J}_\parallel$, $\mathcal{J}_\perp$ are the principal moments of inertia of the decaying system with particle and residual nucleus just in contact, about an axis parallel and perpendicular to the disintegration axis respectively; $\mathcal{J}_c$ is the moment of inertia of the compound nucleus.

Similarly, the neutron decay width, integrated over all the neutron emission directions is

$$\Gamma_N = \Gamma_N^\circ \exp\left[-\frac{\hbar^2 I^2}{2T}\left(\frac{1}{\mathcal{J}_N} - \frac{1}{\mathcal{J}_C}\right)\right] \tag{93}$$

In this expression $\mathcal{J}_N = \mathcal{J}_R + \mu R^2$, corresponding to $\mathcal{J}_\perp$ in Eq. (92), is the sum of the moment of inertia of the residual nucleus after neutron decay and the orbital moment of inertia of the neutron at the surface of the nucleus.

Let us now express the particle decay width in terms of the emission angle α measured with respect to the angular momentum direction.

Since $K = I\cos\alpha$ and $dK = I\, d(\cos\alpha) = I\, d\Omega$, we obtain:

$$\Gamma^I(\alpha)\, d\Omega = \Gamma^\circ \exp\left[-\frac{\hbar^2 I^2}{2T}\left(\frac{1}{\mathcal{J}_\perp} - \frac{1}{\mathcal{J}_C}\right)\right] \exp -\frac{I^2\cos^2\alpha}{2K_o^2}\, d\Omega$$

If the angular momentum has an arbitrary orientation with respect to our chosen frame of reference, defined by its components I_x, I_y, I_z, the angular distribution can be easily rewritten by noticing that

$$K = I\cos\alpha = \underset{\sim}{I}\cdot\underset{\sim}{n} = I_x \sin\theta\cos\phi + I_y \sin\theta\sin\phi + I_z\cos\theta$$

where $\underset{\sim}{n}$ is a unit vector pointing the direction of particle emission with polar angles θ,ϕ. If the orientation of the angular momentum is controlled by the distribution

$$P(\underset{\sim}{I}) \propto \exp - \left[\frac{I_x^2}{2\sigma_x^2} + \frac{I_y^2}{2\sigma_y^2} + \frac{(I_z - \bar{I}_z)^2}{2\sigma_z^2}\right] \tag{94}$$

we can integrate over the distribution of orientations and we obtain, dropping angular momentum independent factors:

$$\Gamma^I(\theta,\phi)\, d\Omega \propto \left[\exp - \frac{\hbar^2 I^2}{2T}\left(\frac{1}{\mathcal{I}_1} - \frac{1}{\mathcal{I}_c}\right)\right] \frac{1}{S(\theta,\phi)} \exp\left(-\frac{I^2\cos^2\theta}{2S^2(\theta,\phi)}\right) d\Omega \qquad (95)$$

where:[22]

$$S^2(\theta,\phi) = K_0^2 + (\sigma_x^2 \cos^2\phi + \sigma_y^2 \sin^2\phi) \sin^2\theta + \sigma_z^2 \cos^2\theta \qquad (96)$$

In the above expression (95) have set $I_z = I$, in other words we have averaged over the orientation but we have allowed the decay width to depend only upon the average angular momentum set equal to its z component. This expression should then be considered only as a high angular momentum limit ($\sigma/I \ll 1$).

The final angular distribution is obtained by integration over the fragment angular momentum distribution which we assume to reflect the entrance channel angular momentum distribution through the rigid rotation condition:

$$\frac{d\sigma}{d\Omega} \propto \int_{I_{min}}^{I_{mx}} 2I\, dI\, \frac{\Gamma^I}{\Gamma_N} \qquad (97)$$

where we have assumed $\Gamma_T = \Gamma_N$. More precisely:

$$W(\theta,\phi) \propto \int_{I_{min}}^{I_{mx}} \frac{2I}{S} \exp\left[- I^2 \frac{\cos^2\theta}{2S^2} - \beta\right] dI \tag{98}$$

or

$$W(\theta,\phi) = \frac{1}{S}\left[\frac{I_{min}^2}{A_{min}} \exp(-A_{min}) - \frac{I_{min}^2}{A_{mx}} \exp(-A_{mx})\right] \tag{99}$$

If $I_{min} = 0$, then:

$$W(\theta,\phi) = \frac{1}{SA}\left[1 - \exp(-A)\right]$$

where

$$A = A_{mx} = I_{mx}^2\left[\frac{\cos^2\theta}{2S^2} - \beta\right] \; ; \quad A_{min} = I_{min}^2\left[\frac{\cos^2\theta}{2S^2} - \beta\right] \tag{100}$$

$$\beta = \frac{\hbar^2}{2T}\left(\frac{1}{\mathcal{I}_n} - \frac{1}{\mathcal{I}_1}\right)$$

The quantity $\mathcal{I}_n$ is the moment of inertia of the nucleus after neutron emission, $\mathcal{I}_1$ is the perpendicular moment of inertia of the critical shape for the decay (e.g., saddle point).

It is important to notice that the angular momentum dependence of the particle/neutron competition or fission/neutron competition is explicitly taken into account through β. This point seems to have been neglected in recent work on sequential decay.

The final ingredient necessary for an explicit calculation of the angular distributions is the quantity K_o^2. This quantity can be expressed in terms of the principal moments of inertia of the critical configuration for the decay:

$$K_o^2 = \frac{1}{\hbar^2}\left(\frac{1}{\mathcal{J}_{\parallel}} - \frac{1}{\mathcal{J}_{\perp}}\right)^{-1} T = \mathcal{J}_{eff} T \tag{101}$$

For fission $\mathcal{J}_{eff}$ can be taken from the liquid drop calculations of C.P.S.[33] For lighter particle emission, the calculation of $\mathcal{J}_{eff}$ can be worked out trivially. Let m, M, A be the masses of the light, residual and total nucleus. One obtains:

$$\mathcal{J}_{\parallel} = \frac{2}{5} MR^2 + \frac{2}{5} mr^2$$

$$\mathcal{J}_{\perp} = \frac{2}{5} MR^2 + \frac{mM}{A}(R + r)^2 \tag{102}$$

$$\frac{\mathcal{J}_{eff}}{\mathcal{J}_{sph}} = \left(\frac{M}{A}\right)^{5/3}\left[1 + \frac{2}{5}\,\frac{A}{m}\left(\frac{R}{R + r}\right)^2\right]$$

where r and R are the radii of the light particle and residual nucleus respectively.

This result is adequate if m << M and if the charge of the light particle is small. If the charge of the light particle is not negligible, one has to consider the shape polarization induced on the heavy fragment at the ridge point, as discussed in Ref. 11. Since the shape polarization affects the asymptotic kinetic energy of the emitted

particle as well, one can in principle utilize the particle kinetic energy spectra to verify that the shape of the system at the ridge point and its principal momenta of inertia have been properly chosen. Again a more complete discussion on this point is available in Ref. 11.

Now we are in the position to calculate both in-plane and out-of plane anisotropies.

The in plane anisotropy gives:

$$\left.\frac{W(\phi = 90^\circ)}{W(\phi = 0^\circ)}\right|_{\theta=90^\circ} = \left(\frac{K_0^2 + \sigma_x^2}{K_0^2 + \sigma_y^2}\right)^{1/2} \tag{103}$$

Since in most cases K_0^2 is fairly large, or at least comparable with σ_x^2 or σ_y^2 it is difficult to obtain a sizable in-plane anisotropy. Even by letting $\sigma_x = 0$ one needs $\sigma_y^2 = 3\ K_0^2$ just to obtain the anisotropy of 2! The out-of-plane anisotropy is somewhat more complicated:

$$\left.\frac{W(\theta = 90^\circ)}{W(\theta = 0^\circ)}\right|_{\phi=)^\circ} = \frac{1}{\beta}\left(\frac{K_0^2 + \sigma_z^2}{K_0^2 + \sigma_x^2}\right)^{1/2}\left(\beta - \frac{1}{2(K_0^2 + \sigma_z^2)}\right) \tag{104}$$

$$\times \frac{1 - \exp\beta I_{max}^2}{1 - \exp I_{mx}^2\left(\beta - \frac{1}{2(K_0^2 + \sigma_z^2)}\right)}$$

For a fixed angular momentum I one has:

$$\left.\frac{W(\theta = 90^\circ)}{W(\theta = 0^\circ)}\right|_{\phi = 0^\circ} = \left(\frac{K_0^2 + \sigma_z^2}{K_0^2 + \sigma_x^2}\right)^{1/2} \exp \frac{I^2}{2(K_0^2 + \sigma_z^2)} \qquad (105)$$

At $\phi = 90^\circ$ the anisotropy is obtained from the above equation by interchanging σ_x with σ_y.

5.2 Some Calculations for Sequential Fission and Alpha Decay and Comparison with Data

The results obtained above can be illustrated by applying them to a reaction which has been experimentally investigated. We choose the reaction 600 MeV ^{86}Kr + Au. For this reaction we estimate $I_{sph}/I_{eff} = 1.864$, $K_0^2 = 100\ \hbar^2$, $\beta = 0.00194\ \hbar^{-2}$, $I_{mx} = 40\hbar$, $\sigma^2 \simeq 110\ \hbar^2$. In order to simultaneously appreciate the shapes of the in- and out-of-plane angular distributions possible in sequential fission, we have artificially set $\sigma_x^2 = 0$, $\sigma_y^2 = \sigma_z^2 = 110\ \hbar^2$. The results are shown in Fig. 18. In this figure one readily appreciates the connection between the in-plane and the out-of-plane angular distributions. In particular, it is apparent how an in-plane anisotropy must necessarily be associated with a variation of the out-of-plane width with the in-plane angle.

We have stressed already that the competition between fission and neutron decay must be dealt with specifically because of the strong dependence of Γ_F upon angular momentum. This is illustrated in Fig. 19 where we have set $\sigma_x^2 = \sigma_y^2 = \sigma_z^2 = 110\ \hbar^2$ and we have assumed $\beta = 0.00194\ \hbar^{-2}$ in one case, and $0.000\ \hbar^{-2}$ in the other. The effect is quite dramatic, and clearly must be incorporated in the formalism if

one intends to obtain reliable angular momentum values from it. For instance, in order to compensate for setting $\beta = 0.000$ instead of $0.00194\ \hbar^{-2}$ it is necessary to step-up the angular momentum I_{mx} from 40 to 55 $\hbar$.

The predicted FWHM = 54° can be compared with the data shown in Fig. 20. The agreement is quite satisfactory.

The present calculations can be compared to those in Ref. 23 where no angular momentum distribution is assumed and thus no neutron competition is included. In the same work no fluctuation in the z component of angular momentum is allowed. Neglection of σ_z ($\sigma_z = 0$) cannot be directly translated into a variation in the angular momentum, because of the difference in the functional dependence. However, a decrease of I_{mx} from $I_{mx} = 40\ \hbar$ to $I_{mx} = 34\ \hbar$ approximately compensates for setting $\sigma_z = 0$. This range of more than 20 $\hbar$ illustrates how dependent is the inferred fragment angular momentum upon the inclusion of angular momentum fluctuations about the z axis and upon the inclusion of neutron competition. Extreme caution is obviously in order when the extracted angular momenta are compared with theoretical predictions, like the rigid rotation limit.

In the same spirit as for sequential fission we show some calculations for sequential alpha decay in the reaction 664 MeV ^{84}Kr + Ag.^{24} The alpha particles are assumed to be emitted by the Ag-like nucleus. We estimate $I_{mx} = 36\ \hbar$, $\sigma^2 = 68\ \hbar^2$, $\beta = 0.00137\ \hbar^{-2}$ and $K_0^2 = 365\ \hbar^2$. The results are shown in Fig. 21. For comparison a calculation with $\sigma^2 = 0$ is also shown in order to illustrate the sensitivity to misalignment. Examples of fits to experimental data are shown in Fig. 22.

The deformation of the deep-inelastic complex was estimated from the measured frgment kinetic energies. Within the framework of two equally deformed spheroids with no neck the fragment energies are given by

$$E_L = \frac{M_H}{M_L + M_H}\left(\frac{Z_L Z_H}{d} F + \frac{l_{rel}^2 \hbar^2}{2\mu d^2}\right) \quad .$$

Here, the Coulomb correction factor (F), the distance between center (d), and the relative angular momentum (l_{rel}) are deformation dependent. In Fig. 23a the experimental fragment energies (plus signs) are compared to calculated values (curves) using the above equation for several deformations. This comparison indicates that assuming the spheroid model a ratio of axis of about two is needed to reproduce the data.

The rms spin values of the large fragment (I_H) extracted by the procedure described above are plotted in Fig. 23b. The strong increase in spin with increasing asymmetry is clear evidence of rigid rotation. Comparing these points to the rigid rotation calculations again indicates the need for large deformations in order to correctly reproduce the magnitude of I_H.

In Fig. 23c the sum of the spins of both fragments as determined by two independent methods are compared to rigid-rotation calculations. In the first method rigid-rotation is invoked to determine I_L from the value of I_H extracted from the out-of-plane alpha distributions. In

the second method, we utilized the experimental gamma multiplicity in the relation.

$$I_L + I_H = 2(M_\gamma - 5) + \Delta$$

to determine the sum of the spins. The corrections Δ for the angular momentum removed by neutrons and alpha particles which were done following the prescription described in Ref. 25. The agreement between the M_γ derived spins and those derived from the out-of-plane α-distributions is quite good.

These data provide the first unambiguous evidence for rigid rotation of the intermediate complex in this mass region. Furthermore, large spheroidal deformations are indicated by three sources: fragment kinetic energies, spins extracted from alpha distributions and those deduced from gamma multiplicity data. It should be mentioned that methods of reproducing the fragment kinetic energies employing smaller deformations and a separation or thin neck fail to convert enough orbital angular momentum into intrinsic spins to be consistent with the angular momentum data.

5.3 Gamma ray angular distributions

Fragments with large amounts of angular momentum are expected to dispose of it mainly by stretched E2 decay. The relative amounts of dipole and quadrupole radiation depends mainly upon the ability of the nucleus to remain a good rotor over the whole angular momentum range.

If the angular momentum of the fragment is aligned, the typical angular pattern of the quadrupole radiation should be observed. Any misalignment should decrease the sharpness of the angular distribution.

If the distribution of the angular momentum components I_x, I_y, I_z is statistical, it is straightforward to derive analytical expressions for the angular distributions.[21]

For a perfectly aligned system we have:

$$W(\alpha) = \frac{3}{4}(1 + \cos^2\alpha) \quad ; \quad W(\alpha) = \frac{5}{4}(1 - \cos^4\alpha) \tag{106}$$

for E1 for E2

If the angular momentum is not aligned with the z axis, one must express α in terms of θ, ϕ which define the direction of the angular momentum vector. In particular we have:

$$\cos\alpha = \frac{\underset{\sim}{I}\cdot\underset{\sim}{n}}{I} = \frac{I_x \sin\theta\cos\phi + I_y \sin\theta\sin\phi + I_z\cos\theta}{(I_x^2 + I_y^2 + I_z^2)^{1/2}} \tag{107}$$

For any given I, the angular distribution is obtained by integration over the statistical distribution $P(\underset{\sim}{I})$ of the angular momentum components:

$$W(\theta,\phi) = \int W(\alpha)\, P(\underset{\sim}{I})\, d\underset{\sim}{I} \tag{108}$$

It is not possible to obtain exact analytical expression for the general case. However, an expansion to order $\sigma_x^2/\bar{I}_z^2$, $\sigma_y^2/\bar{I}_z^2$, etc. allows one to obtain expressions in closed form.

For the dipole decay we have:

$$W(\theta,\phi) = \frac{3}{4}(1 + \cos^2\theta) + \frac{3}{4}\left[(\sin^2\theta \cos^2\phi - \cos^2\theta) \frac{\sigma_x^2}{\bar{I}_z^2} + (\sin^2\theta \sin^2\phi - \cos^2\theta) \frac{\sigma_y^2}{\bar{I}_z^2}\right] \tag{109}$$

Notice that there is no dependence upon σ_z^2. In the case in which $\sigma_x = \sigma_y = \sigma$, we obtain the simplified expression:

$$W(\theta,\phi) = \frac{3}{4}(1 + \cos^2\theta) + \frac{3}{4}(\sin^2\theta - 2\cos^2\theta) \frac{\sigma^2}{\bar{I}_z^2} \tag{110}$$

A weak in-plane anisotropy is possible:

$$\frac{W(\phi = 0^\circ)}{W(\phi = 90^\circ)_{\theta=90^\circ}} = \frac{1 + \sigma_x^2/\bar{I}_z^2}{1 + \sigma_y^2/\bar{I}_z^2} \cong 1 + \frac{\sigma_x^2 - \sigma_y^2}{\bar{I}_z^2} \tag{111}$$

The out-of-plane anisotropy is:

$$\frac{W(0^\circ)}{W(90^\circ)} \simeq 2\,\frac{(1 - \sigma^2/\bar{I}_z^2)}{(1 + \sigma^2/\bar{I}_z^2)} \simeq 2(1 - 2\sigma^2/\bar{I}_z^2) \tag{112}$$

For the quadrupole decay we have:

$$W(\theta,\phi) = \frac{5}{4}\,(1 - \cos^4\theta) - \frac{5}{2}\left[(3\sin^2\theta\cos^2\theta\cos^2\phi - \cos^4\theta)\,\frac{\sigma_x^2}{\bar{I}_z^2}\right.$$

$$\left. + (3\sin^2\theta\cos^2\theta\sin^2\phi - \cos^4\theta)\,\frac{\sigma_y^2}{\bar{I}_z^2}\right] \tag{113}$$

Again, no dependence upon σ_z^2 is predicted. If one assumes $\sigma_x = \sigma_y = \sigma$ as before, one obtains:

$$W(\theta) = \frac{5}{4}\,(1 - \cos^4\theta) - \frac{5}{2}\,(3\sin^2\theta\cos^2\theta - 2\cos^4\theta)\,\sigma^2/\bar{I}_z^2 \tag{114}$$

and

$$\frac{W(0^\circ)}{W(90^\circ)} \simeq 4\,\frac{\sigma^2}{\bar{I}_z^2} \tag{115}$$

For the in plane anisotropy we have:

$$\left.\frac{W(\phi = 0^\circ)}{W(\phi = 90^\circ)}\right|_{\theta=90^\circ} \sim 1 \tag{116}$$

to order $\sigma^2/\bar{I}_z^2$. This can be easily understood. The rms misalignment is $\sim\sigma/I$, thus, at $\theta = 90^\circ$:

$$W(90) = 1 - \cos^4 90° - \frac{\sigma}{I} \simeq 1 - \frac{\sigma^4}{I^4}$$

Thus, no second order term exists. This result shows that its is very difficult to study anistropies in the angular momentum misalignment by means of γ-ray angular distribution.

The range of validity of the above expressions is rather limited due to the low order expansion. In particular, the equations should not be trusted for $\sigma^2/\bar{I}_z^2 > 0.05$.

However, if we are willing to assume $\sigma_x^2 = \sigma_y^2 = \sigma_x^2$, then an exact result can be obtained.

For the E1 distribution one obtains:

$$W(\theta)_{E1} = \frac{3}{4}\left[1 + \cos^2\theta + \beta^2(1 - D(\beta))(1 - 3\cos^2\theta)\right] \tag{117}$$

For the E2 distribution one obtains:

$$\begin{aligned} W(\theta)_{E2} = \frac{5}{4}\Big[1 - \cos^4\theta - 2\beta^2 \Big\{ & 3\sin^2\theta\cos^2\theta - 2\cos^4\theta \\ & - \frac{3}{4} D(\beta)(\sin^2\theta - 4\cos^2\theta)\sin^2\theta \Big\} + \\ & - 3\beta^4 \Big\{ 4\cos^4\theta + \frac{3}{2}\sin^4\theta - 12\sin^2\theta\cos^2\theta \Big\}(1 - D(\beta))\Big] \end{aligned} \tag{118}$$

In these equations $\beta = \sigma/\bar{I}_z$ and $D(\beta) = \sqrt{2}\ \beta\ F(1/\sqrt{2}\ \beta)$ where

$$F(x) = e^{-x^2} \int_0^x e^{t^2} dt$$

is the Dawson's integral. One can verify immediately that both expressions behave as expected in the limits of $\beta = 0$ and $\beta = \infty$. In Fig. 24 one can verify that the anisotropy $W(0)/W(90^\circ)$ tends to 1 when β tends to infinity both for E1 and E2 transitions, while it tends to ~ for E2 and to 2 for E1 when $\beta = 0$. For convenience of calculations, we give here an expansion of these equations up to 8^{th} order in β which is adequate up to $\beta^2 \leq 0.4$

For E1 we obtain:

$$W(\theta) = \frac{3}{4}\left[1 + \cos^2\theta + (1 - 3\cos^2\theta)(\beta^2 - \beta^4 - \beta^6 - 3\beta^8)\right] \tag{119}$$

$$\frac{W(0^\circ)}{W(90^\circ)} \simeq \frac{2 - 2\beta^2 + 2\beta^4 + 2\beta^6 + 6\beta^8}{1 + \beta^2 - \beta^4 - \beta^6 - 3\beta^8}$$

Similarly, for E2 we obtain:

$$W(\theta)_{E2} \simeq \frac{5}{4}\Big[1 - \cos^4\theta - 2\beta^2\{3\sin^2\theta\cos^2\theta - 2\cos^4\theta\} - 3\beta^4\{4\cos^4\theta + \sin^4\theta - 10\sin^2\theta\cos^2\theta\} + 6\beta^6\{2\cos^4\theta + \sin^4\theta - 7\sin^2\theta\cos^2\theta\} + 3\beta^8\{3\sin^4\theta + 4\cos^4\theta - 18\sin^2\theta\cos^2\theta\}\Big] \qquad (120)$$

$$\frac{W(0^\circ)}{W(90^\circ)} \simeq \frac{4\beta^2(1 - 3\beta^2 + 3\beta^4 + 3\beta^6)}{(1 - 3\beta^4 + 6\beta^6 + 9\beta^8)}$$

It is recommended that these last equations be used instead of eqs. (110, 112, 114 and 116) in actual calculations.

These results are graphically summarized in Fig. 25 where the anisotropy is plotted as a function of the fraction of E1 radiation for various values of $\sigma^2/\bar{I}^2$. The two extreme possibilities of stretched and non-stretched E1 decay are considered. If one has a fairly good experimental idea of the amount of E1 radiation to be expected from a given fragment and of its degree of stretching, the measurement of the anisotropy yields directly the value of σ^2/I^2, which is of course the most direct information about the misalignment.

5.4 Gamma Ray Anisotropy Experiments.

a) The 1060 MeV Xe + Au Experiment[26]

The predictions of the model just described can be compared with the γ-ray anistropy measured for the above system. A window in mass was set in the neighborhood of symmetric splitting, in order to consider fragments in the heavy rare-earth region which are good rotors and for which the amount of dipole radiation has been measured

to be ~20 percent. The temperature of the system at symmetry is estimated to be T ≈ 2 MeV, and

$$\sigma^2 \approx \frac{\mathcal{I}T}{\hbar^2} = 140 \quad .$$

In the absence of angular momentum fractionation, the rms fragment spin should be $I_F \approx 46\ \hbar$. However, the measured γ-ray multiplicity yields $I \approx 32\ \hbar$ indicating that fractionation occurs along the mass asymmetry coordinate and that the lower l-waves have a better chance to reach symmetry. Thus the misalignment parameter is $\sigma^2/I^2 \approx 0.14$. With 20 percent E1 transitions, Fig. 25 predicts anisotropies close to 0.70. The experimental results, shown in Fig. 26 indicate that such an anisotropy is indeed observed in the region of gamma ray energies where the quadrupole bump is observed.

b) The 1400 MeV ^{165}Ho + ^{165}Ho experiment.[27]

This system was chosen because large amounts of angular momentum can be transferred into the intrinsic spin (I) of these nuclei, which are known to have good rotational properties.[28,29] Furthermore, the steep mass-asymmetry potential causes the reaction products to lie within a narrow range of Z-values centered around symmetry (as verified with a ΔE-E telescope) and minimizes l-fractionation effects.[30] As a consequence, both of the essentially identical DI-fragments emit similar continuum γ-ray spectra which are strongly enriched in E2 transitions (~80 percent) as discussed below.

A schematic diagram of the experimental setup is shown as an insert in Fig. 7.

Figure 27(a) illustrates the general features of both the in-plane and out-of-plane γ-ray spectra emitted from the reaction fragments. The spectral shapes are similar to those observed in compound-nucleus reactions[28,29] and display the characteristic "E2 bump" at 0.6-1.2 MeV and the higher energy "statistical tail" (2-5 MeV). A comparison of these two spectra indicates that the tail region is nearly isotropic, as seen in compound-nucleus reactions, whereas the "bump" region is more pronounced in-plane where the angular distribution for stretched E2 transitions peaks.

In-plane γ-ray energy spectra, normalized so that the integral of each curve is equal to $\langle M_\gamma \rangle$, are shown in Fig. 27(b) for several Q-value regions. The upper edge of the "bump" moves to higher γ-ray energies as Q increases in the quasi-elastic (QE) region and stabilizes in the DI-region. This is an indication of the Q-value dependence of the angular momentum transfer, since for rotational nuclei $E_\gamma \propto I$.

The angle-integrated γ-ray multiplicity was calculated from

$$\langle M_\gamma \rangle = N_\gamma / [W(90^\circ) N_{singles}]$$

where N_γ is the efficiency-corrected number of coincident γ-rays. The angular-distribution function, $W(\theta)$, is normalized such that $\int W(\theta)\, d\Omega = 4\pi$, and $N_{singles}$ is the number of particle singles. The fragment spin after particle emission was calculated from

$$\langle I \rangle = \frac{1}{2} (I_1 + I_2) = \langle M_\gamma \rangle + 2H - 2B$$

where H is the number of E2 transitions below the 0.3 MeV threshold (set to exclude backscatter region) and B is the number of statistical transitions per fragment. We assumed that the statistical transitions carry away no angular momentum on the average, and selected the value H = 3 after inspecting the γ-decay schemes of even- and odd-mass products between A = 165 and A = 150.

Figure 28(a) shows the fragments' energy spectrum obtained at an angle slightly greater than the grazing angle. Figure 28(b) shows the intrinsic spin of one of the two reaction fragments after neutron emission (circles) as calculated from the above equation. The primary fragment spin obtained from $\langle M_\gamma \rangle$ with correction for neutron emission[25] (solid line) is also shown. As seen in the data, the transferred spin rapidly increases with Q-value in the QE-region and saturates at about 35ħ in the DI-region.

The ratio of in-plane to out-of-plane γ-ray yield ("anisotropy") for energies between 0.6 and 1.2 MeV (squares) is also shown in Fig. 28(b). This anisotropy rises with increasing spin transfer; it peaks at a value of ~2.2, slightly before the spin saturates, and then drops to near unity for large Q-values. Figure 28(c) shows the dependence of the anisotropy on both E_γ and Q in two-dimensional contour diagram. One notes that the highest anisotropy occurs in the 0.6 to 1.2 MeV E_γ region, where the "E2 bump" is most prominent, and at intermediate Q-values. At higher Q-values, anisotropy is at higher E_γ. These trends are consistent with the statistical nature of these γ-ray spectra.

The initial rise of anisotropy with increasing Q-value indicates that during the early stages of energy damping there is a rapid build-up of aligned spin. The subsequent fall observed at larger Q-values suggests that the aligned component of spin has saturated or is decreasing, whereas randomly-oriented components continue to increase, causing a significant decrease in the alignment of the fragments' spin. These qualitative features are similar to those observed with discrete lines from the $^{16}O + {}^{48}Ti$ system.[31] However, in this much heavier system, the rise and fall of the alignment is observed over a substantially larger Q-value range with continuum γ-rays. This buildup of alignment has also been seen in sequential-fission studies,[32] but a decrease was not observed in the more limited Q-value range studied.

Interpretation of these data may be approached in several ways, e.g., dynamical models, non-equilibrium statistical mechanics, etc. We choose to utilize the statistical equilibrium model described above. Corrections have been made[25] for contributions from the secondary depolarization process of neutron evaporation which precedes the γ-ray cascade.

Figure 29(a) shows experimental values of the anisotropy for E_γ greater than 0.3 MeV compared to several stages of the model calculation. The number of statistical transitions per fragment, B, was estimated from the shape of the γ-ray spectra for each Q-value bin assuming that the intensity of the statistical transitions is described by:[29] $P(E_\gamma) \propto E_\gamma^2 \exp(-E_\gamma/T)$, where T = 0.6 MeV. With this value for

B, the measured $\langle M_\gamma \rangle$, and H = 3, the spin $\langle I \rangle$ was determined from Eq. (2), and the anisotropy was then calculated (Fig. 28(a)), solid line). This calculation reproduces both the shape and the magnitude of the data. To give a feeling for the importance of various contributions, the same calculation is shown with no correction for neutron evaporation (curve 2), assuming no statistical transitions (curve 3), and with no thermal effects (curve 4). This comparison clearly shows that the most important effect is the thermally induced misalignment, indicating that the decrease of alignment as deduced from the anisotropy is inherent to the deep-inelastic process itself. The misalignment due to statistical γ-ray emission is negligible ($\sigma^2 \sim 3\hbar^2$).

By gating on the 0.6-1.2 MeV region of the E_γ spectra, one both increases the fraction of E2-transitions and biases the spin distribution to larger values ($E_\gamma \propto I$), which should yield larger anisotropies. In Fig. 29(b), measured (symbols) and calculated (solid line) anisotropies are shown for the 0.6-1.2 MeV γ-ray region. These data show the expected larger anisotropies, which the model calculations reproduce. The model prediction (corresponding to the solid line) of the alignment parameter $P_{ZZ} = (3\ \langle I_Z^2 \rangle / 2 \langle I^2 \rangle - 1/2)$ before neutron emission is 0.74 for the Q-value associated with the largest anisotropy and decreases to 0.58 for the largest Q-value.

The above γ-ray multiplicity and anisotropy data in conjunction with the model calculations give rise to the following picture of the reaction process. In the QE-region, the transferred spin increases rapidly with Q-value whereas the thermally misaligned components increase more slowly

($T \propto |Q|^{1/2}$). Thus, the aligned component dominates and the transferred angular momentum is nearly perpendicular to the reaction plane, giving a large anisotropy. However, across the DI-region the transferred angular momentum saturates while the thermal components increase to become an ever larger fraction of the total angular momentum. Thus, the alignment decreases and the anisotropy plummets.

6. CONCLUSION

It is a good custom of a polite speaker, especially if he has spoken long and tedious hours, to sum up at the end by making strong references to the title and the introduction. Such a technique tries to achieve two goals. On the one hand it may make those who slept away the tedium feel that they have got the gist of the talk and have not lost much. On the other, it gives the speaker the opportunity of conveying a semblance of unity and coherence to the preceding disorganization and chaos. Also, the organizers usually gain the feeling that this was indeed what they wanted the speaker to speak about.

With these hopes, we may try to sum up by observing that heavy ion reactions do produce nuclei of rather unusual shapes and sizes and give rise to a variety of phenomena that make the delight of experimenters and theorists alike. And if old Plato thumbs his nose in disgust, we may answer that all those symmetries of his may be beautiful but boring. This is why most people praise heaven but act as if they do not want to go there (by the way, heaven is another Platonic archetype smuggled into

Christianity by well meaning Hellenists). And yet, we have ended up paying respect to Plato, in a way, when, in trying to make some theoretical sense out of experimental nonsense, we have modelled nuclei with rather symmetric shapes, like cylinders, two-touching spheres and the like. On the other hand, to avoid the wrath of the organizers, we have carefully avoided sphere and Platonic solids. As a last message, one might point out how tremendously useful statistical mechanics has proven itself to be in dealing with all these heavy ion processes. A Nobel laureate friend of mine who shares with me the Italian accent and mycological interests, rightly says that "Holy thermodynamics never fails." Now this is another archetypal hang-up of Greek origin. It started up with Epicurus and was picked-up by Lucretius who developed the subject very poetically in "De rerum natura." But this is a conclusion and the name Epicurus is best associated with what goes on after the lectures.

This work was supported by the Nuclear Science Division of the U.S. Department of Energy under Contract W-7405-ENG-48.

REFERENCES

1. L. G. Moretto, J. Sventek and G. Mantzonuranis, Phys. Rev. Lett. 42 563 (1979).
2. G. Wirth, W. Bruchle, H. Gaggeler, J. V. Kratz, M. Schadel, I. Warneke, G. Hermann, M. Weis, R. Lucas, J. Poitou, Hirschegg (1979) p. 13.
3. M. Berlanger, A. Gobbi, F. Hanappe, V. Lynen, C. Ngo, A. Olmi, H. Sann, H. Steltzer, H. Richel and M. F. Rivet., Z. Physik A291 133 (1979).
4. L. G. Moretto, C. R. Albiston and G. Mantzouranis, Phys. Rev. Lett. 44, 924 (1980).
5. See for instance Nifenecker, preprint.
6. R. Reginbart, A. Behkami, G. J. Wozniak, R. P. Schmitt, J. J. Sventek, and L. G. Moretto, Phys. Rev. Lett. 41 1355 (1978).
7. M. M. Aleonard, G. J. Wozniak, P. Glassel, M. M. Deleplanque, R. M. Diamond, L. G. Moretto, R. P. Schmitt and F. S. Stephens, Phys. Rev. Lett. 40 622 (1978).
8. P. Glässel, R. S. Simon, R. M. Diamond, R. C. Jared, I. Y. Lee, L. G. Moretto, J. O. Newton, R. Schmitt and F. Stephens, Phys. Rev. Lett. 38 331 (1977).
9. J. B. Natowitz, N. M. Namboodiri, P. Kasiraj, R. Eggers, L. Adler, P. Goutier, C. Cerutti and T. Alleman, Phys. Rev. Lett. 40 751 (1978) .
10. L. G. Moretto and R. P. Schmitt, Phys. Rev. C21, 204 (1980).
11. L. G. Moretto, Nucl. Phys. A247, 211 (1975).

12. L. G. Moretto, J. Galin, R. Babinet, Z. Fraenkel, R. Schmitt, R. Jared, and S. G. Thompson, Nucl. Phys. A259, 172 (1976).

13. B. Heusch, C. Volant, H. Freiesleben, R. P. Chestnut, K. D. Hildenbrand, F. Puhlhofer, W. F. W. Schneider, B. Kohlmeyer, and W. Pfeffer, Z. Physik A288, 391 (1978).

14. J. Galin, B. Gatty, D. Guerrean, M. Lefort, X. Tarrago, S. Agarwal, R. Babinet, B. Cauvin, J. Girard and H. Nifenecker, Z. Physik A283, 173 (1977).

15. M. Beckerman and M. Blann, Phys. Rev. Lett. 38, 272 (1977).

16. P. Christensen, F. Folkmann, O. Hansen, O. Nathan, N. Trautner, F. Videbaek, S. Y. van der Werf, H. C. Britt, R. P. Chestnut, H. Freiesleben, and F. Puhlhofer, Phys. Rev. Lett. 40 1245 (1978).

17. J. S. Sventek, private communication.

18. S. Ayik, G. Wolschin and W. Norenberg, Z. Physik A286, 271 (1978).

19. J. R. Nix and W. J. Swiatecki, Nucl. Phys. 71, 1 (1965).

20. G. J. Wozniak, R. P. Schmitt, P. Glassel, R. C. Jared, G. Bizard and L. G. Moretto, Phys. Rev. Lett. 40, 1436 (1978).

21. L. G. Moretto, S. K. Blau and A. Pacheco, LBL-10805.

22. R. A. Broglia, G. Pollarolo, C. H. Dasso and T. Dossing, Phys. Rev. Lett. 43, 1649 (1979).

23. B. B. Back and S. Bjornholm, Nucl. Phys. A302, 343 (1978).

24. L. G. Sobotka, C. C. Hsu, G. J. Wozniak, G. V. Rattazzi, R. J. McDonald, A. Pacheco and L. G. Moretto, LBL-11148.

25. S. K. Blau and L. G. Moretto, LBL-10926.

26. P. Aguer, G. J. Wozniak, R. P. Schmitt, D. Habs, R. M. Diamond, C. Ellegaard, D. L. Hillis, C. C. Hsu, G. J. Mathews, L. G. Moretto, G. U. Rattazzi, C. P. Roulet, and F. Stephens, Phys. Rev. Lett. 43 1778 (1979) .

27. G. J. Wozniak, R. J. McDonald, A. Pacheco, C. C. Hsu, D. J. Morrissey, L. G. Sobotka, L. G. Moretto, S. Shih, C. Schuck, R. M. Diamond, H. Kluge and F. S. Stephens LBL-11196.

28. M. A. Deleplanque, et al., Phys. Rev. Lett. 41, 1105 (1978).

29 F. S. Stephens, Lawrence Berkeley Laboratory Report No., 10356, published in the Proc. of the Varenna Conf., July 1979.

30. M. Aleonard, et al., Phys. Rev. Lett. 40, 622 (1978).

31. H. Puchta, et al., Phys. Rev. Lett. 43, 623 (1979).

32. R. J. Puigh, et al., Phys. Lett. 86B, 24 (1979).

33. S. Cohen, F. Plasil and W. J. Swiatecki, Ann. Phys. (N.Y.) 82 (1974) 557.

FIGURE CAPTIONS

Fig. 1 Variances of the Z distributions at fixed mass asymmetry vs. excitation energy in the reaction ^{136}Xe + Au. The dashed and solid curves indicate the expected variance from quantal and classical statistical fluctuations.(2)

Fig. 2 Widths of the Z distributions for several masses vs. total kinetic energy for the reaction ^{86}Kr + ^{98}Mo.(3)

Fig. 3 The stiffness constant for the oscillation of the charge excess is plotted against asymmetry ($Q = A_1/A_{total}$) for A = 100. The dashed curve corresponds to the liquid drop potentials for two touching spheres. The solid curve corresponds to the cylinder model for the lowest mode. The Coulomb term is included in both calculations.(4)

Fig. 4 The square of the normalized partial width is plotted a) against asymmetry at fixed n; b) against n at fixed asymmetry.(4)

Fig. 5 The sum of the squares of the normalized partial widths up to n_{max} is plotted against asymmetry.(4)

Fig. 6 Gamma ray multipliciy vs. total kinetic energy for three Kr induced reactions. The solid and dashed curves are fit to the data.(6)

Fig. 7 Gamma ray multiplicities vs. Z for the quasi elastic components of the reactions ^{165}Ho, ^{197}Au + 618 MeV ^{86}Kr.(7)

Fig. 8 Gamma ray multiplicities for the reaction 175 MeV ^{20}Ne + Ag at 90° Lab,[8] and for the reaction 237 MeV ^{40}Ar + ^{89}Y.[9]

Fig. 9 Gamma ray multiplicities vs. Z for the deep inealstic components in 618 MeV ^{86}Kr + ^{nat}Ag, ^{165}Ho, ^{197}Au.[7]

Fig. 10 Gamma ray multiplicity vs. Z for three reactions. The open circles represent the quasi elastic components and the solid circles the deep inelastic components. Solid curves are fit to the data.[6]

Fig. 11 (a) Mass distributions for the indicated reaction obtained by integrating over all l-waves leading to fission (squares) and for selected individual l-waves (solid curves). The l-values are $l = 0$, $l_{mx}/2$ and l_{mx}. All curves have been normalized to unity at symmetry.

(b) Mean (crosses) and mean squares (squares) angular momentum divided by the corresponding quantities obtained by averaging over the l-distribution which leads to fission vs asymmetry. The angular momentum dependence of the temperature and total reaction width have been incorporated into the calculations (see text).

Fig. 12 (a) Same as Fig. 11 but in the absence of neutron competition. Note that only the total mass distribution (squares) is different from Fig. 11(a).

(b) Same as Fig. 11(b) but without neutron competition.

Fig. 13 Mean angular momentum $\langle n \rangle$, its second moment σ, the relative function $\rho = \sigma/\langle n \rangle$ and the skewness γ vs. the asymmetry parameter β (see text). The asterisks represent the expected dependence of the gamma ray multiplicity upon β.[17]

Fig. 14 Total spin of the fragments arising from wriggling as a function of the spin arising from rigid notation alone plotted in dimensionless form. The upper solid curve shows the result for both of the wriggling modes while the lower solid curve corresponds to the excitation of a single wriggling mode (see text). The limiting behavior for both small and large x are indicated in both cases.

Fig. 15 Schematic illustrating the tilting mode and the doubly degenerate wriggling modes for the two equal sphere model. The long arrows originating at the point of tangency for the two spheres is the orbital angular momentum while the shorter arrows represent the individual fragment spins.

Fig. 16 Schematic illustrating the twisting and bending modes for the two equal sphere model. Note the pairwise cancellation of the fragment spins.

Fig. 17 Total fragment spin as a function of the spin arising from rigid rotation for the twisting and bending modes. Dimensionless forms are utilized. The limiting behavior for large and small x are indicated.

Fig. 18 Calculated in-plane and out-of-plane angular distribution for sequential fission in the reaction 600 MeV Kr + Au. The in-plane anisotropy is generated by explicitly setting $\sigma_x = 0$.

Fig. 19 Sequential fission angular distributions for the system 600 MeV Kr + Au. The curve labeled $\beta = 0.0$ corresponds to disregarding neutron emission fission competition. The more realistic curve labeled $\beta = 0.00194$ gives a FWHM of 45°.

Fig. 20 Full width at half maximum of the out-of-plane fission and non-fission components as a function of Z in the reaction 618 MeV $^{86}Kr + ^{197}Au$.(20)

Fig. 21 Calculated out-of-plane angular distribution for sequential alpha decay from the Ag-like fragment in the reaction 665 MeV $^{84}Kr + ^{nat}Ag$ (dashed line). The solid line has been obtained by setting $\sigma = 0$.

Fig. 22 Alpha particle angular distributions for several Z-bins as a function of out-of-plane angle. The Z bins are 3 Z's wide and are indicated by the median Z. In section a) there is no coincident γ-ray requirement while in b) there are 2 or more coincident γ-rays. The curves in section b) are normalized at 90° to those in a) for the same z bin.

Fig. 23 (a) Center of mass energies after evaporation corrections as a function of the charge of the light fragment. Horizontal bars indicate the uncertainty in the primary charge (before evaporation) of the light fragment. Solid lines are calculations for two spheroids in contact and are labeled by the ratio of axes. The broken line is for spheres.

(b) Spin of the heavy fragment extracted from its out-of-plane α-distribution. Calculations for rolling and rigid rotation of spheroids are indicated.

(c) Sum of the spins of the deep inelastic fragments as determined by out-of-plane α-distributions (closed) and M_γ (open).

Fig. 24 (a) Dependence of the gamma-ray anisotropy upon $\sigma^2/\bar{I}_Z^2$ for a mixture of sketched E1 and E1 transitions (see text).

(b) Same as in 24(a), but for a mixture of random E1 and stretched E2.

Fig. 25 (a) Gamma-ray anisotropy for a mixture of stretched E1 and E2 transitions of the fraction of E1 radiation for various values of $\sigma^2/\bar{I}_Z^2$.

(b) Same as in 25(a) but for a mixture of random E1 and stretched E1 transitions.

Fig. 26 (Please observe only left-hand side.) Out-of-plane gamma ray anisotropy as a function of gamma ray energy for the reaction 1064 MeV ^{136}Xe + Au in the product mass range 152 < A < 172 at three different Q-value bins.

Fig. 27 (a) In- and out-of-plane γ-ray pulse-height spectra associated with reaction products having a Q-value of ~ -140 MeV. Data points are shown only for the in-plane spectrum. Detectors NaI(1) and Si(1) are in the same plane. (b) In-plane γ-ray pulse-height spectra for representative Q-value bins.

Fig. 28 (a) Particle spectrum for the $^{165}Ho + ^{165}Ho$ reaction at 27° in the laboratory.

(b) Post- (circles) and pre- (solid line) neutron emission values of the spin per fragment I_1 as a function of the reaction Q-value (see text). The anisotropies, W(in/⊥), extracted from the raw NaI spectra are also shown (squares) for the E_γ region 0.6-1.2 MeV. (The raw data and the unfolded spectra gave the same anisotropies to 5 percent.)

(c) Anisotropy contours for coordinates E_γ and Q.

Fig. 29 Experimental (symbols) and calculated (curves) values of the anisotropy, W(in/⊥), (a) for γ-rays greater than 0.3 MeV and (b) for the region 0.6 MeV < E_γ < 1.2 MeV (see text).

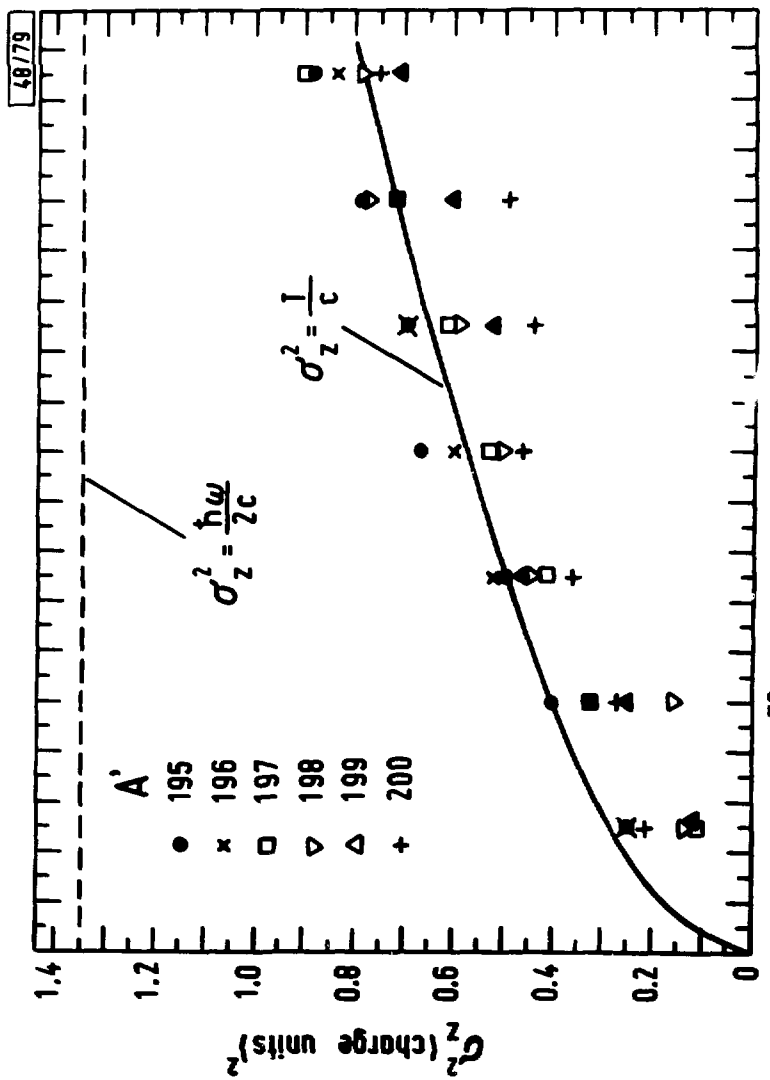

XBL 795-9813

Fig. 1

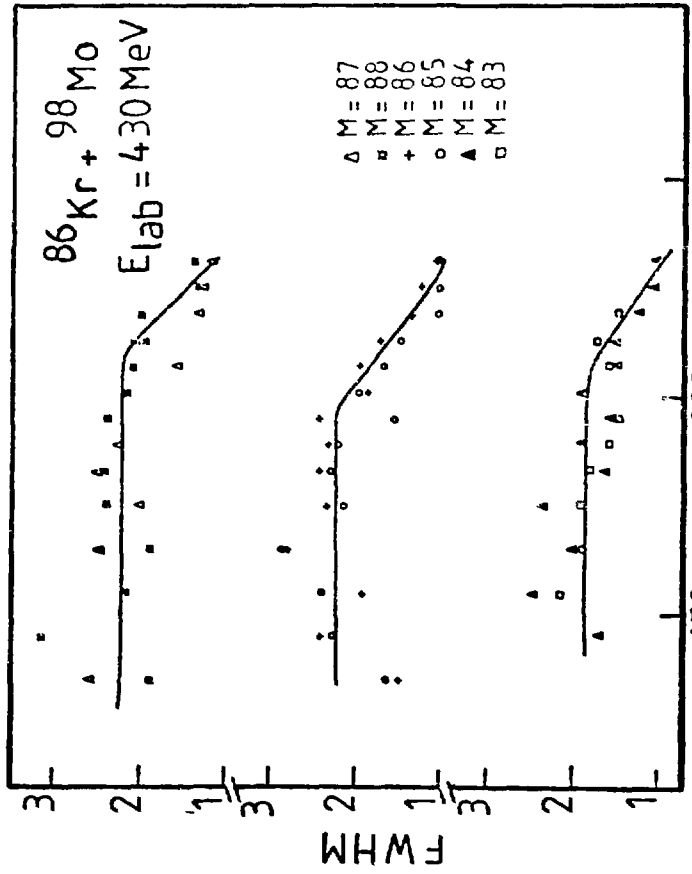

XBL 808-11247

Fig. 2

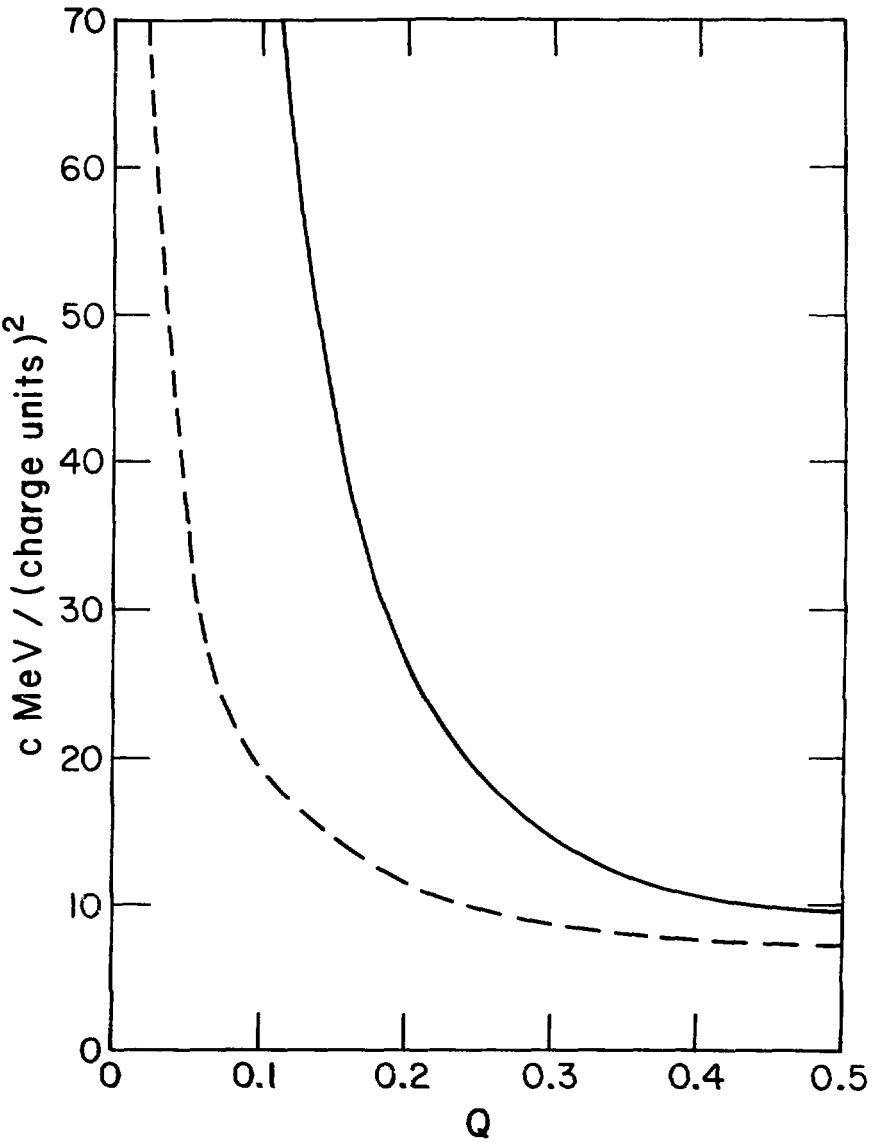
70
60
50
40
30
20
10
0
0
0.1
0.2
0.3
0.4
0.5
Q
c MeV / (charge units)^2
XBL 7910-4422

Fig. 3

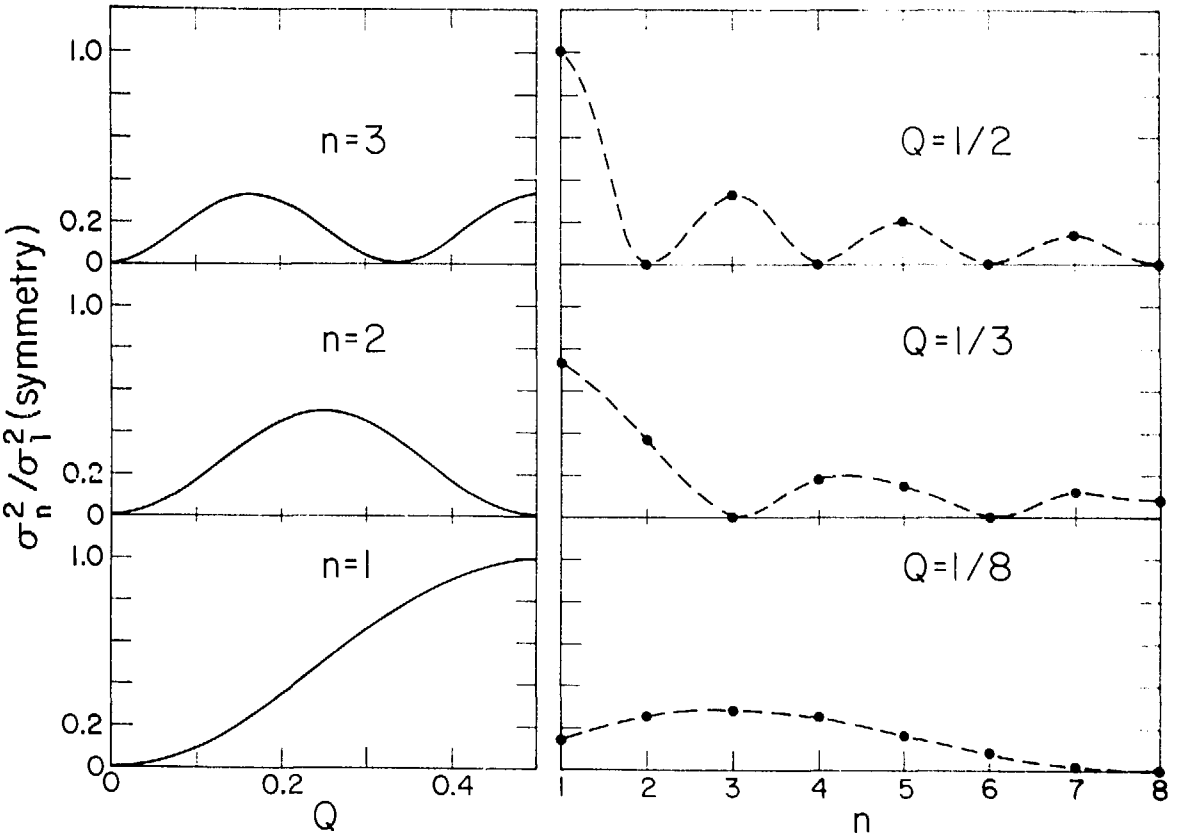

Fig. 4

XBL 7911-4421

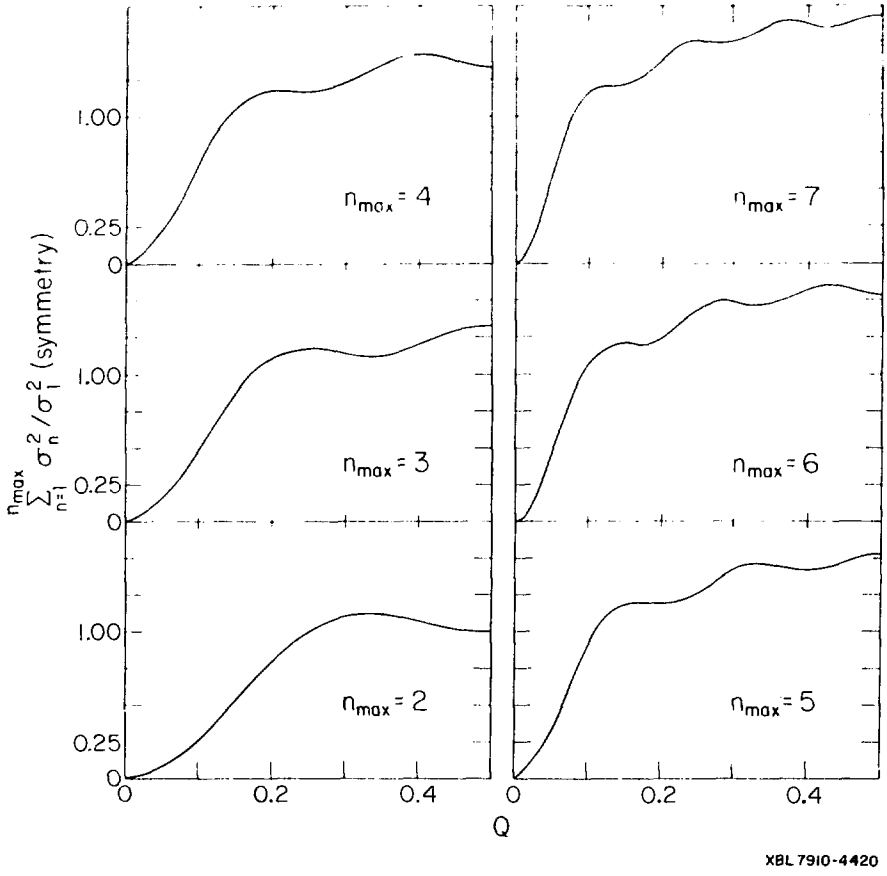
$\sum_{n=1}^{n_{max}} \sigma_n^2/\sigma_1^2$ (symmetry)
1.00
0.25
0
$n_{max} = 4$
$n_{max} = 7$
$n_{max} = 3$
$n_{max} = 6$
$n_{max} = 2$
$n_{max} = 5$
0
0.2
0.4
Q
XBL 7910-4420

Fig. 5

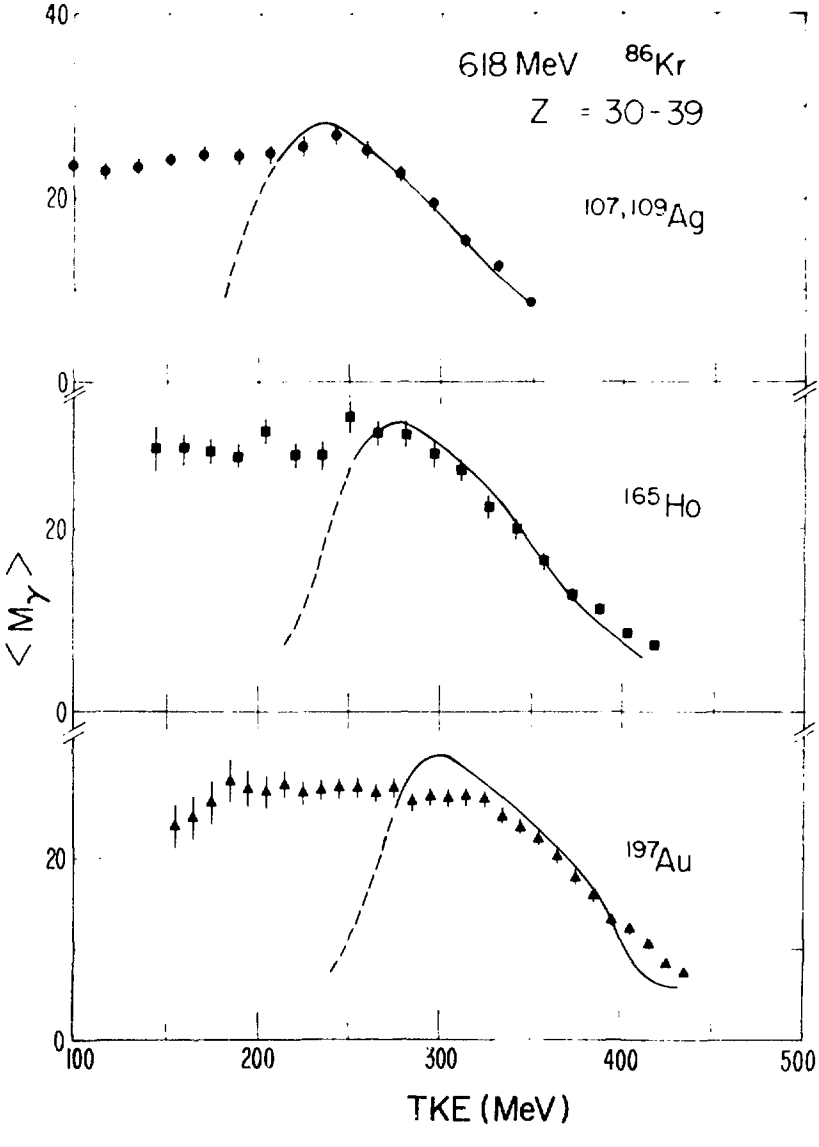

XBL 786-2553

Fig. 6

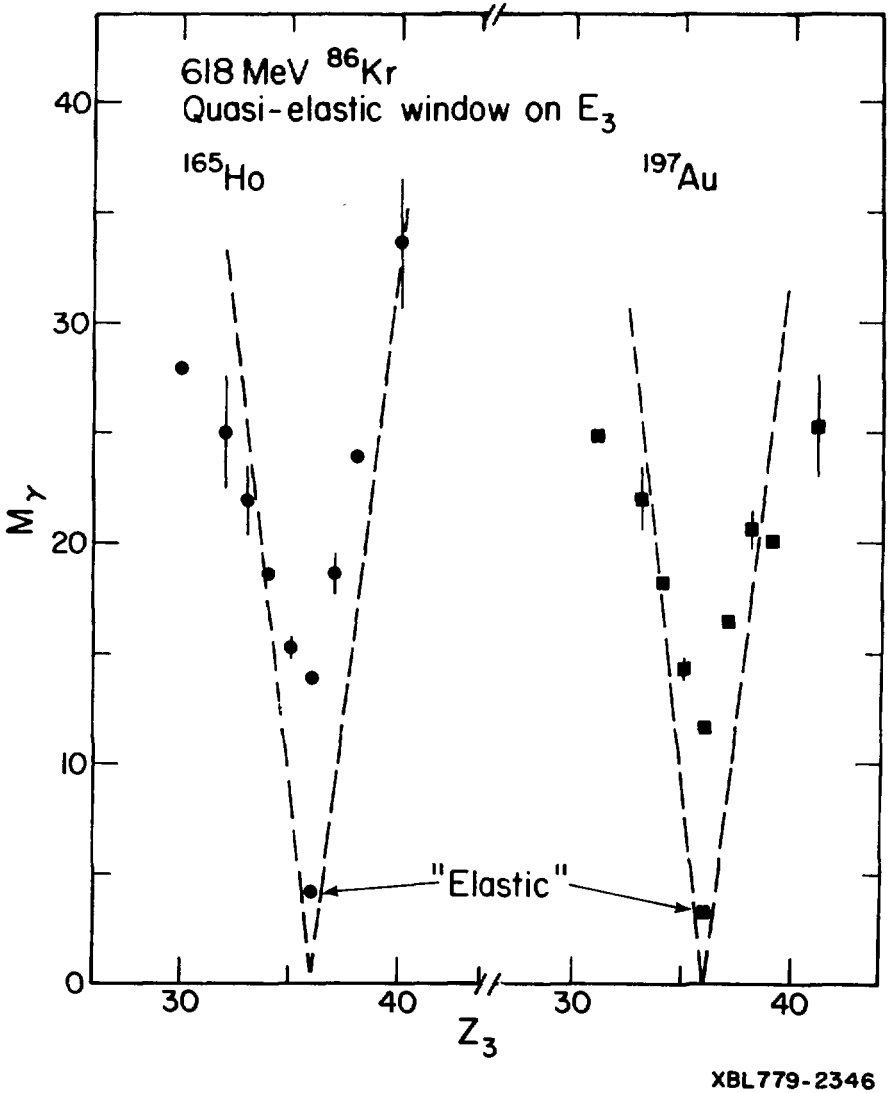
618 MeV ^{86}Kr
Quasi-elastic window on E_3
^{165}Ho
^{197}Au
"Elastic"
M_γ
Z_3
0
10
20
30
40
30
40
30
40
XBL779-2346

Fig. 7

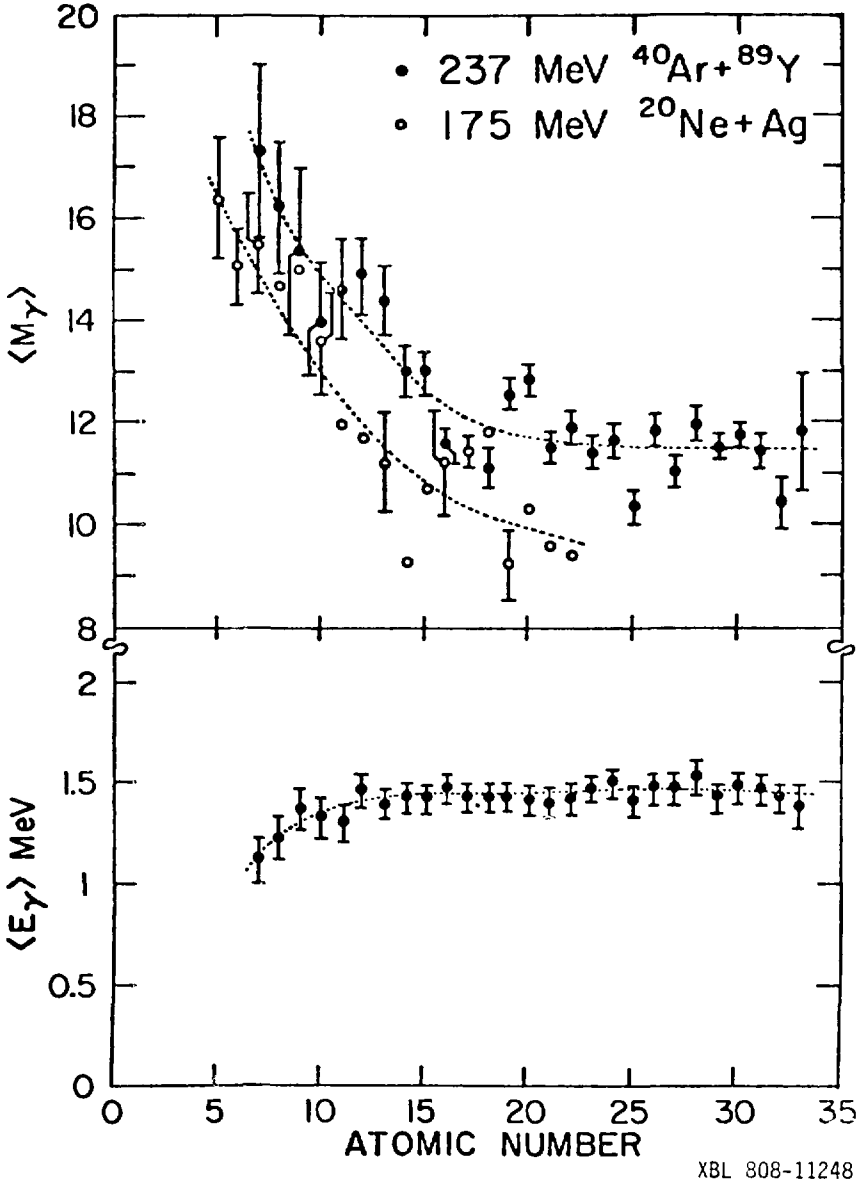
• 237 MeV ^{40}Ar+^{89}Y
○ 175 MeV ^{20}Ne+Ag
⟨M$_\gamma$⟩
⟨E$_\gamma$⟩ MeV
ATOMIC NUMBER
XBL 808-11248

Fig. 8

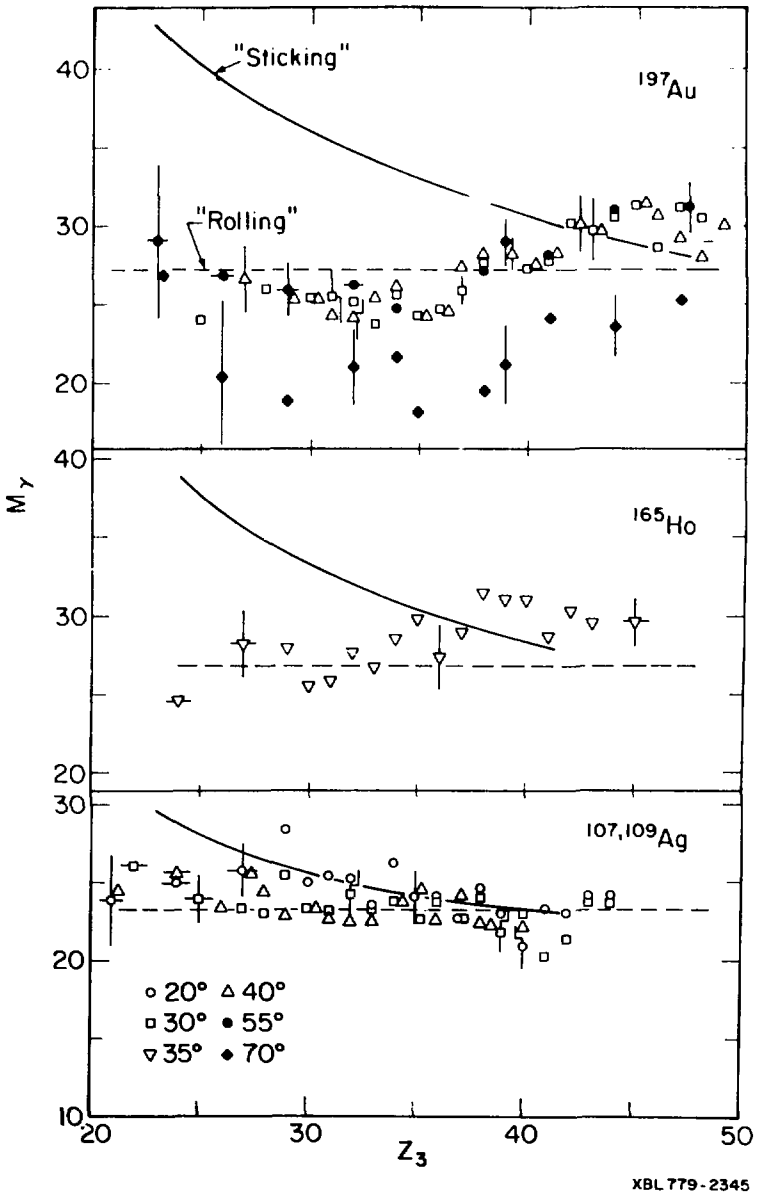
"Sticking"
"Rolling"
197Au
165Ho
107,109Ag
M_Y
Z_3
20°
30°
35°
40°
55°
70°
XBL 779-2345

Fig. 9

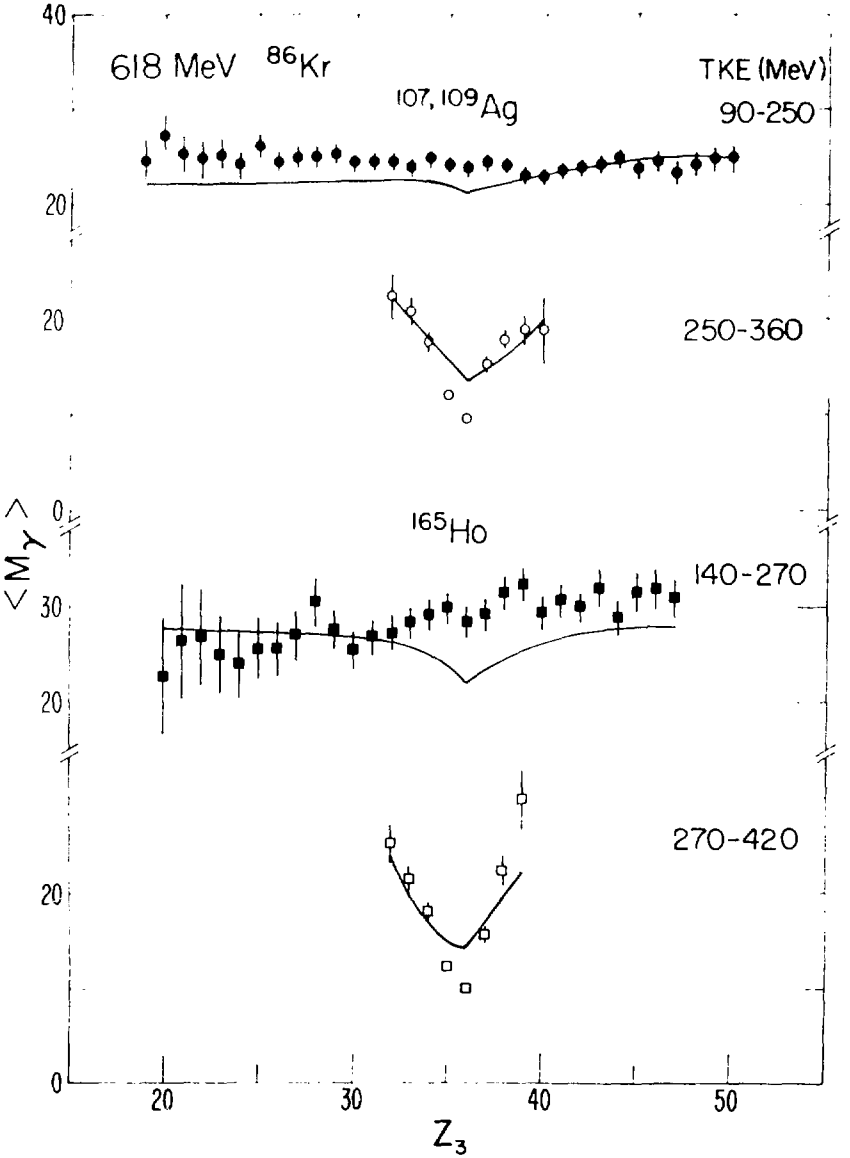

XBL 786-2556

Fig. 10

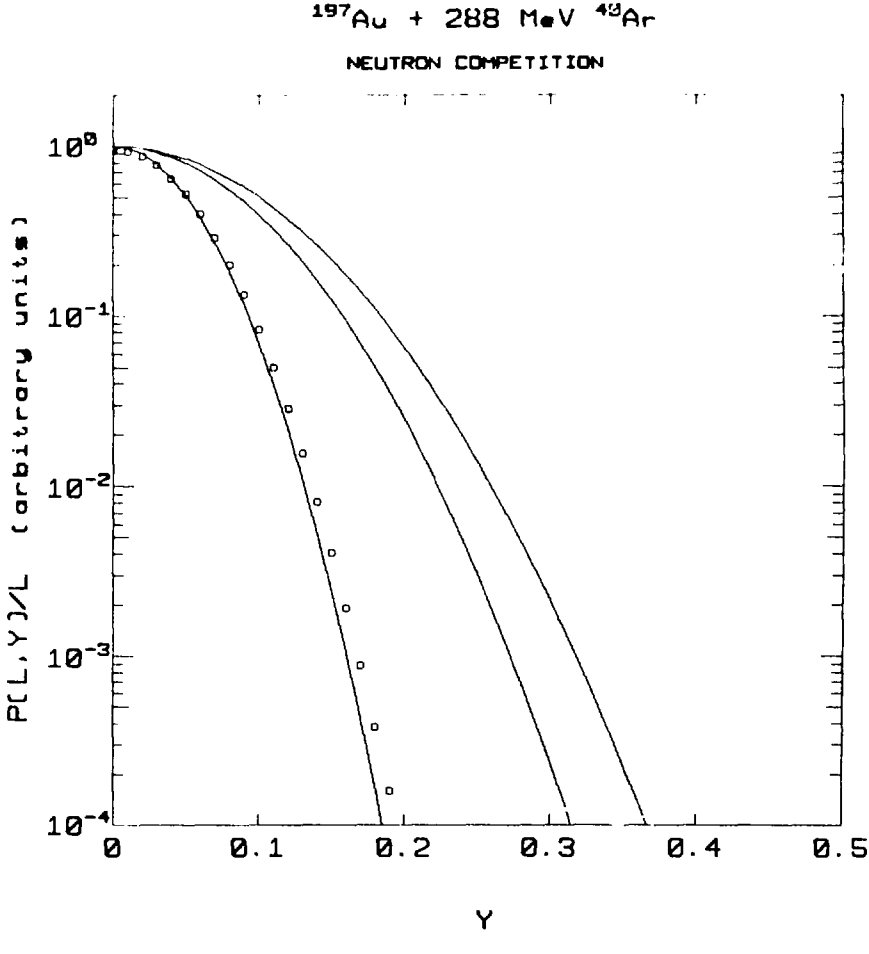
197Au + 288 MeV 40Ar
NEUTRON COMPETITION
P[L,Y]/L (arbitrary units)
10^0
10^-1
10^-2
10^-3
10^-4
0
0.1
0.2
0.3
0.4
0.5
Y
XBL 794-9196

Fig. 11a

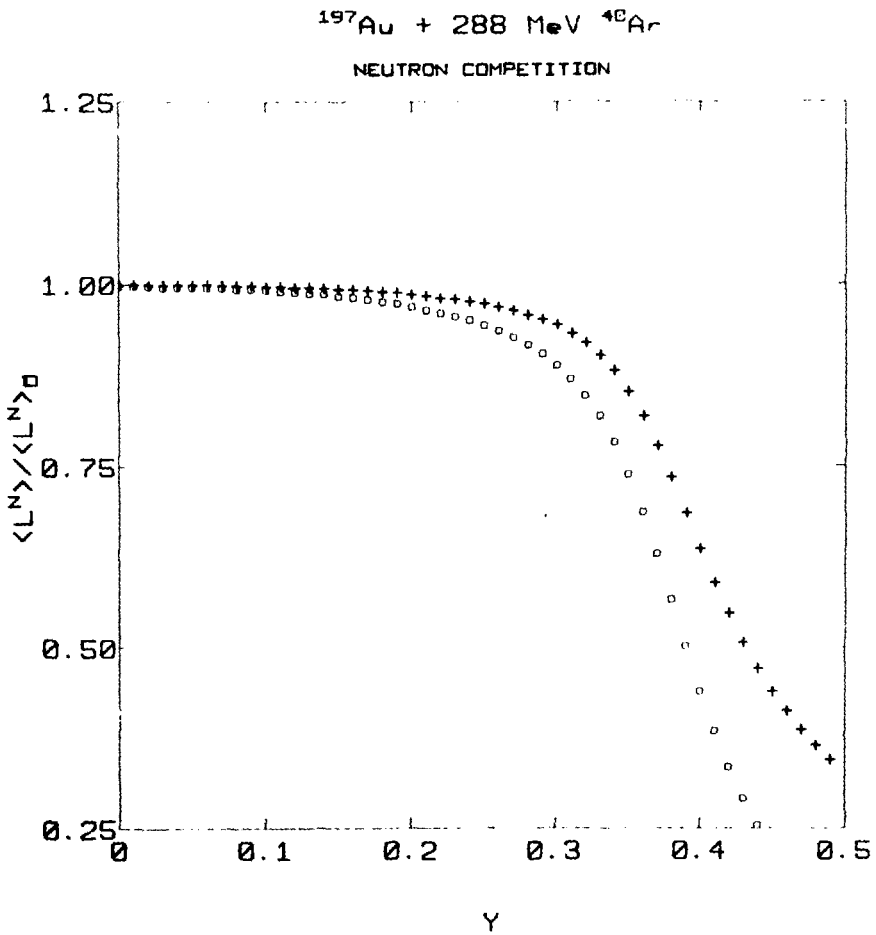

XBL 794-9198

Fig. 11b

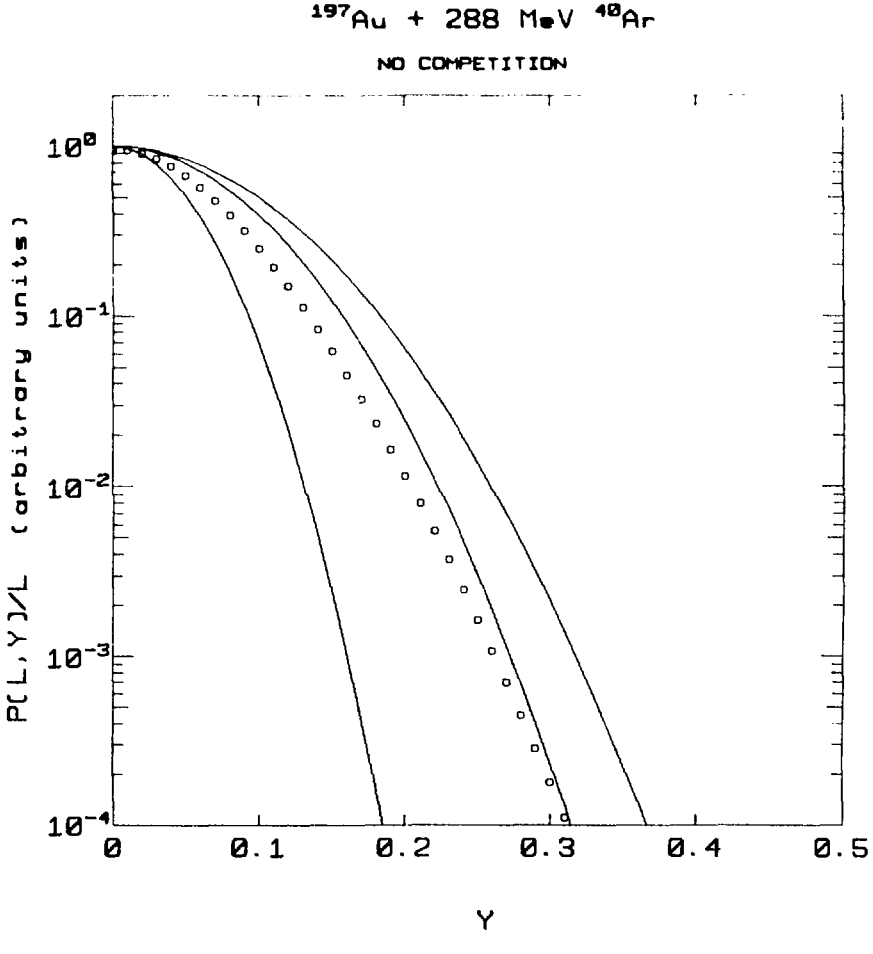
197Au + 288 MeV 40Ar
NO COMPETITION
P[L,Y]/L (arbitrary units)
10^0
10^-1
10^-2
10^-3
10^-4
0
0.1
0.2
0.3
0.4
0.5
Y
XBL 794-9195

Fig. 12a

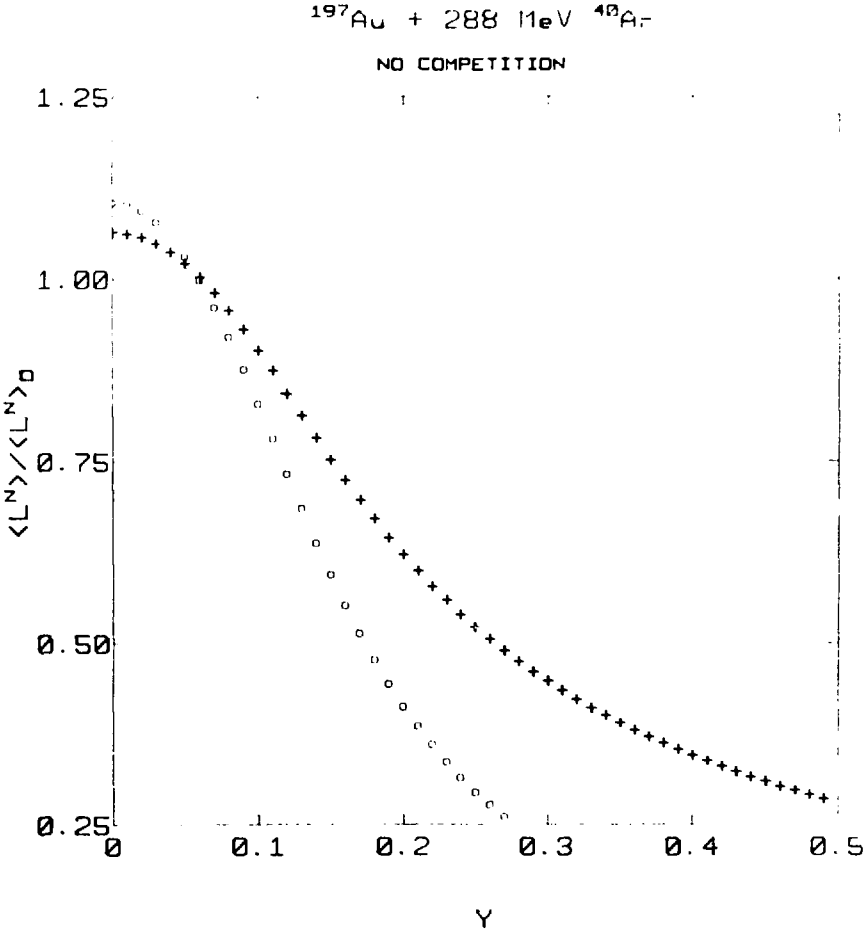

Fig. 12b

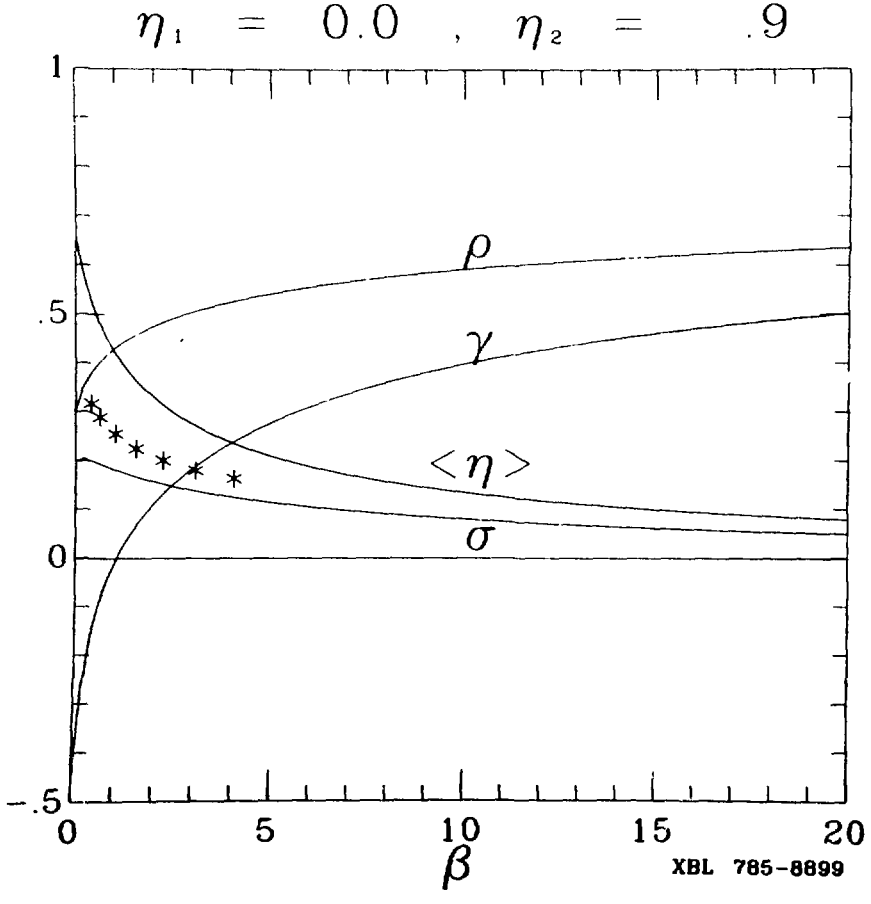
$\eta_1 = 0.0 , \eta_2 = .9$
1
.5
0
-.5
0
5
10
15
20
β
ρ
γ
$<\eta>$
σ
XBL 785-8899

Fig. 13

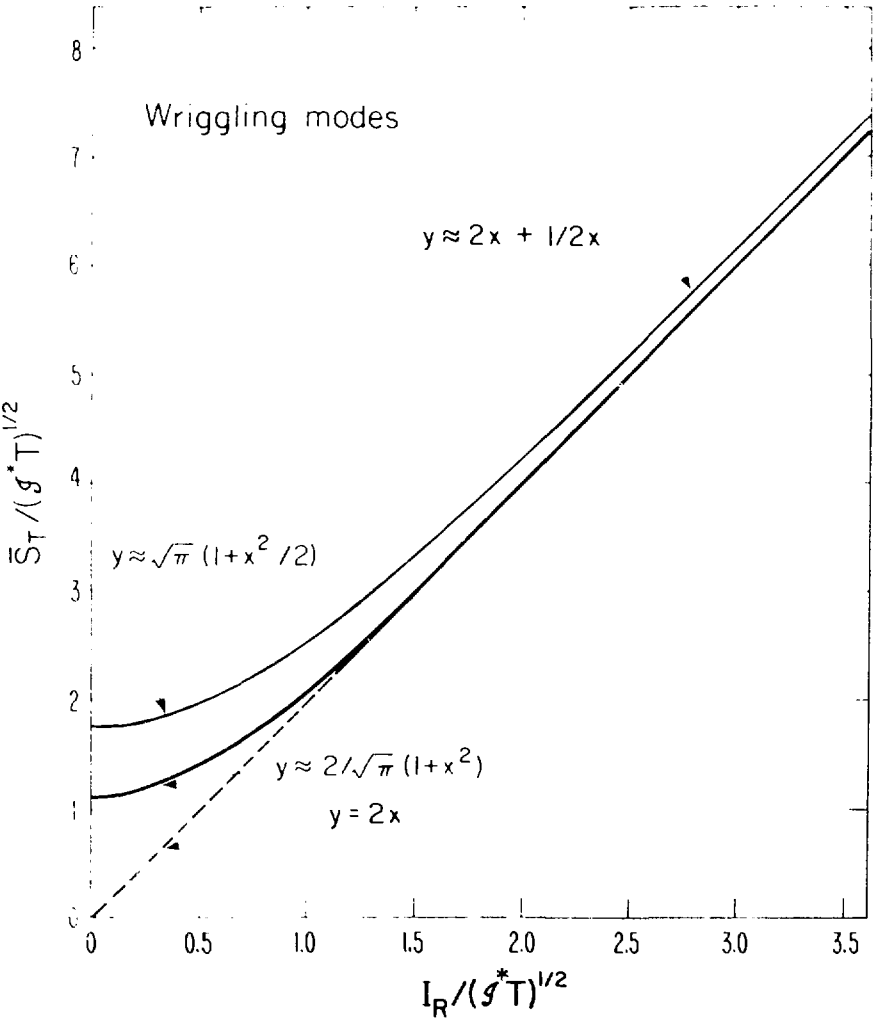

XBL 793-822

Fig. 14

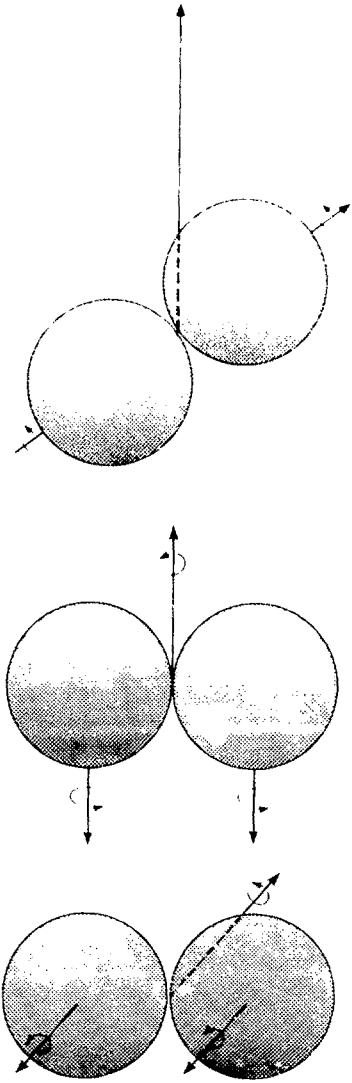

XBL 793-824

Fig. 15

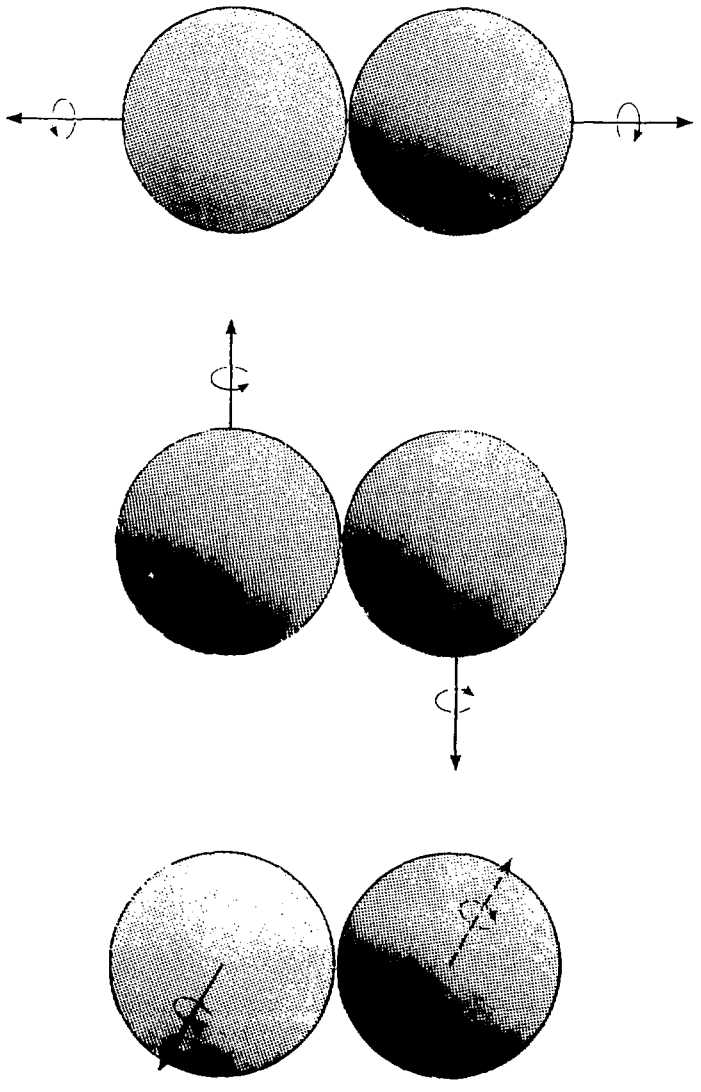

XBL 791-206

Fig. 16

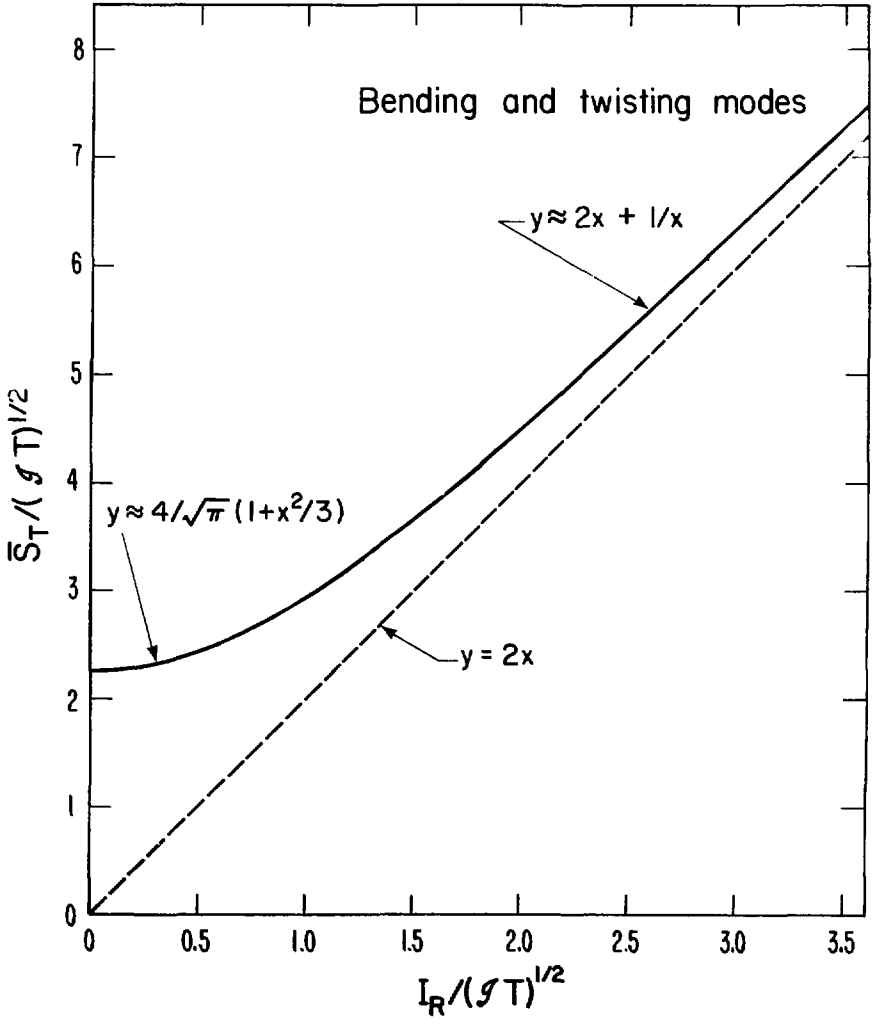

XBL 793-823

Fig. 17

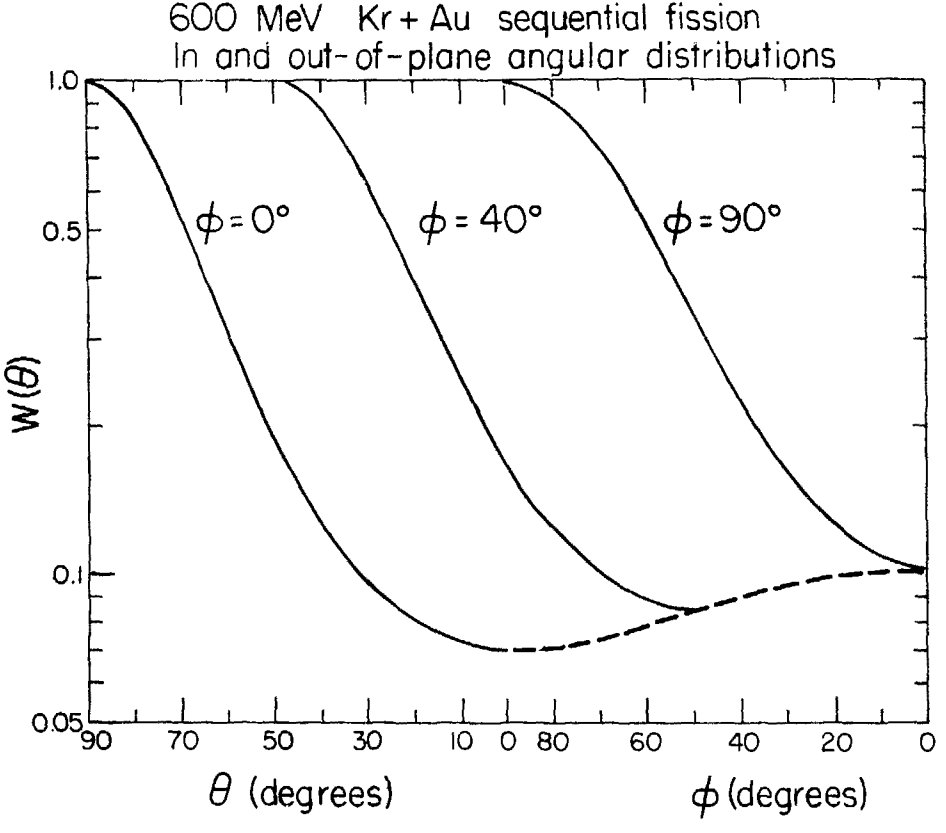

XBL 802-277

Fig. 18

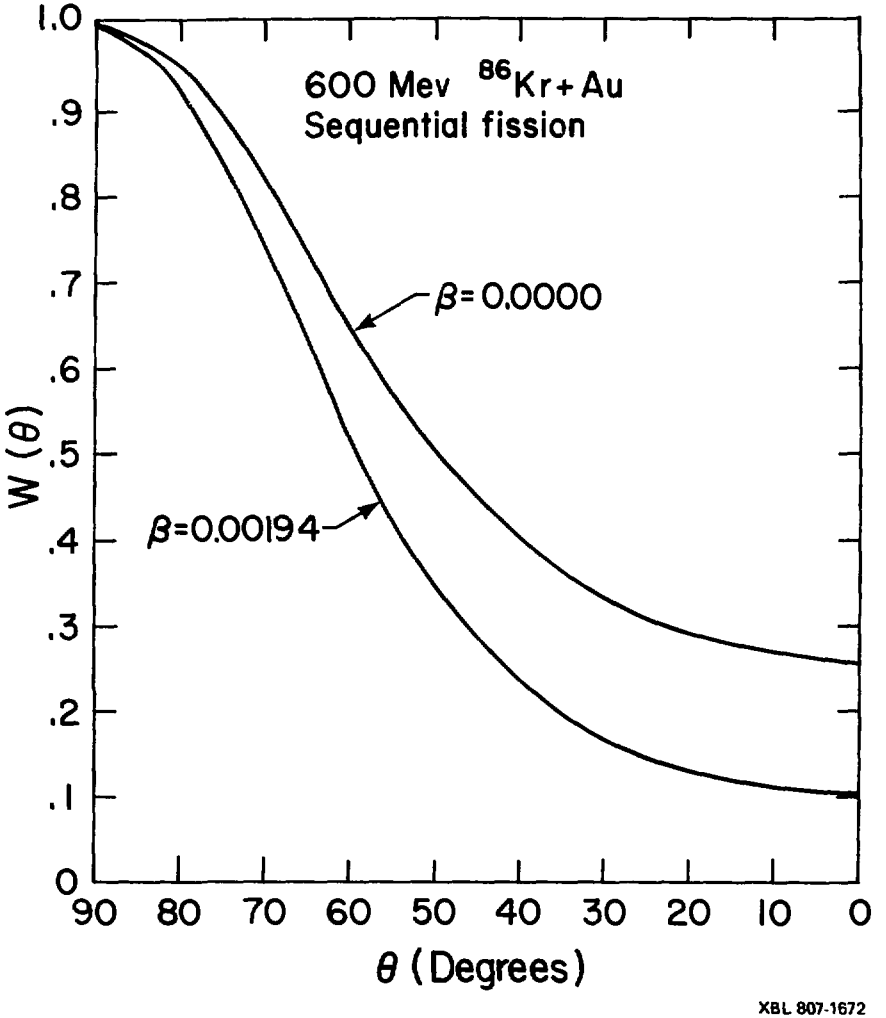
600 Mev ^{86}Kr + Au
Sequential fission
β= 0.0000
β=0.00194
W (θ)
θ (Degrees)
1.0
.9
.8
.7
.6
.5
.4
.3
.2
.1
0
90 80 70 60 50 40 30 20 10 0
XBL 807-1672

Fig. 19

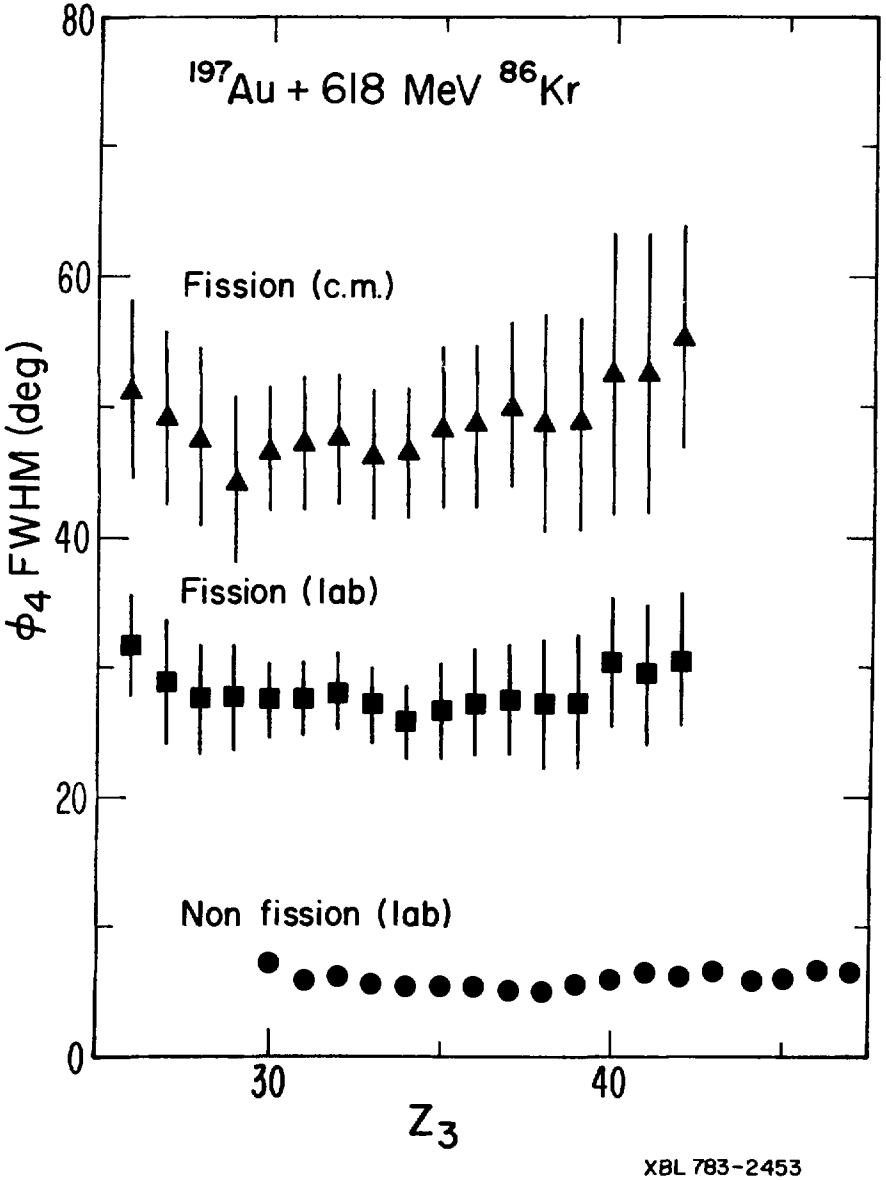
^{197}Au + 618 MeV ^{86}Kr
Fission (c.m.)
Fission (lab)
Non fission (lab)
ϕ_4 FWHM (deg)
Z_3
80
60
40
20
0
30
40
XBL 783-2453

Fig. 20

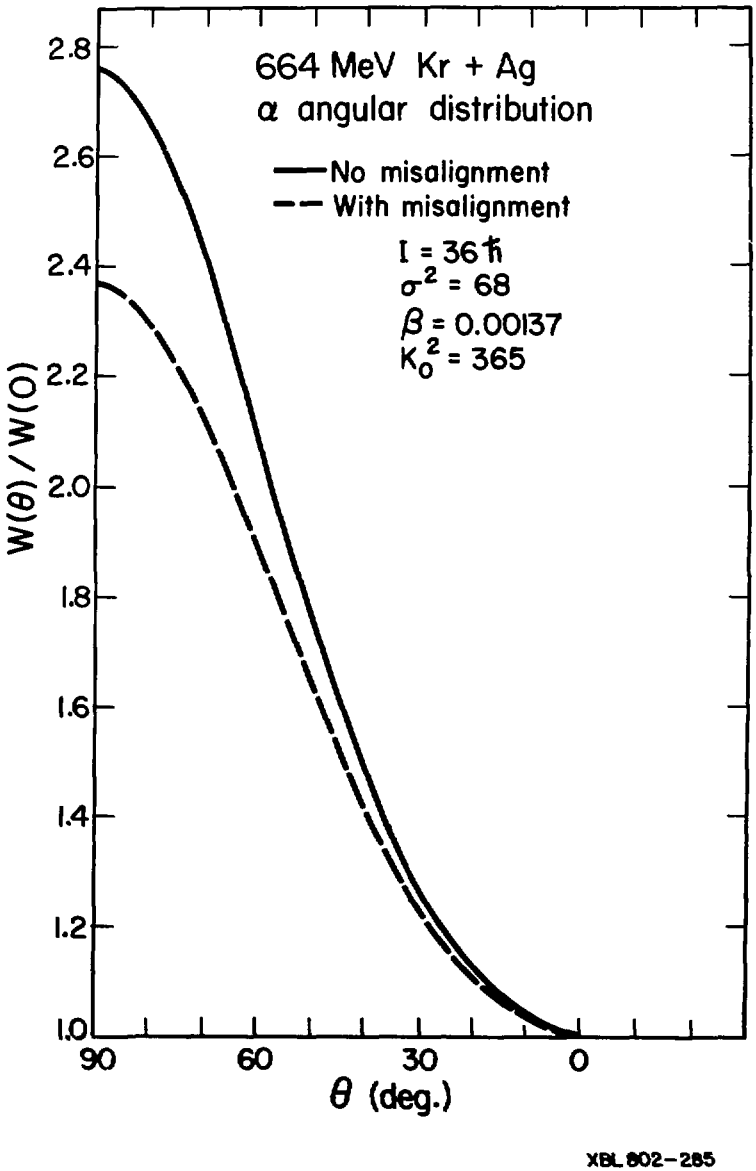

XBL 802-285

Fig. 21

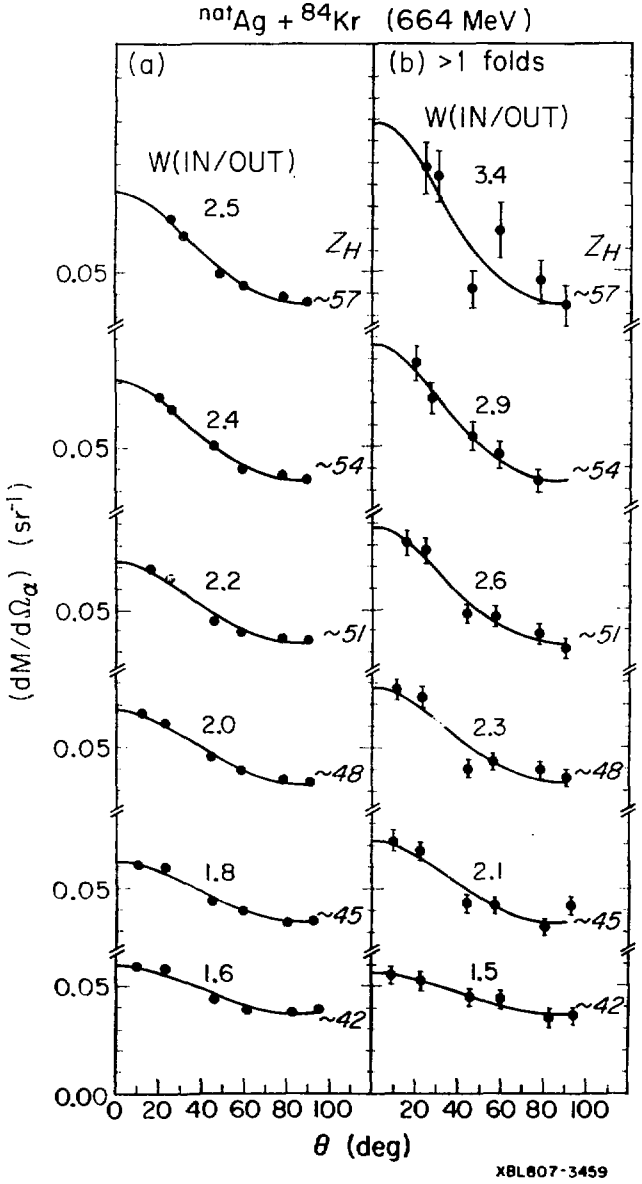
$^{nat}Ag + ^{84}Kr$ (664 MeV)
(a)
(b) >1 folds
W(IN/OUT)
W(IN/OUT)
2.5
3.4
2.4
2.9
2.2
2.6
2.0
2.3
1.8
2.1
1.6
1.5
Z_H
~57
~54
~51
~48
~45
~42
0.05
0.00
0 20 40 60 80 100
20 40 60 80 100
$(dM/d\Omega_\alpha)$ (sr^{-1})
θ (deg)
XBL807-3459

Fig. 22

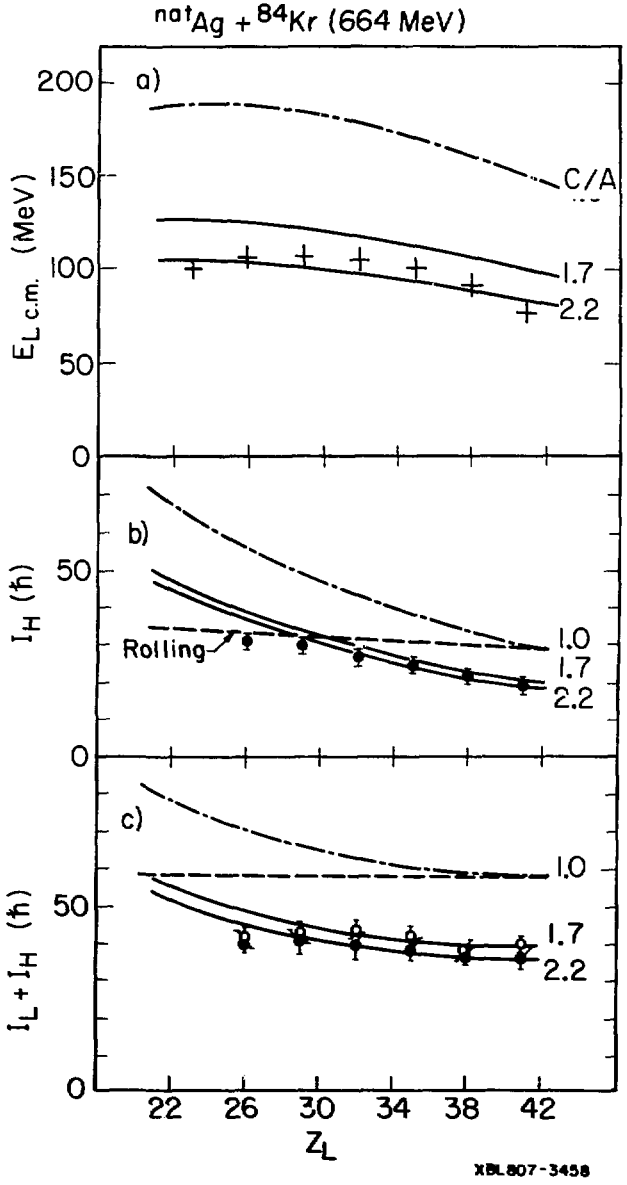
$^{nat}Ag + ^{84}Kr$ (664 MeV)
a)
200
150
100
50
0
$E_{L\,c.m.}$ (MeV)
C/A
1.7
2.2
b)
50
0
I_H ($\hbar$)
Rolling
1.0
1.7
2.2
c)
50
0
$I_L + I_H$ ($\hbar$)
1.0
1.7
2.2
22
26
30
34
38
42
Z_L
XBL807-3458

Fig. 23

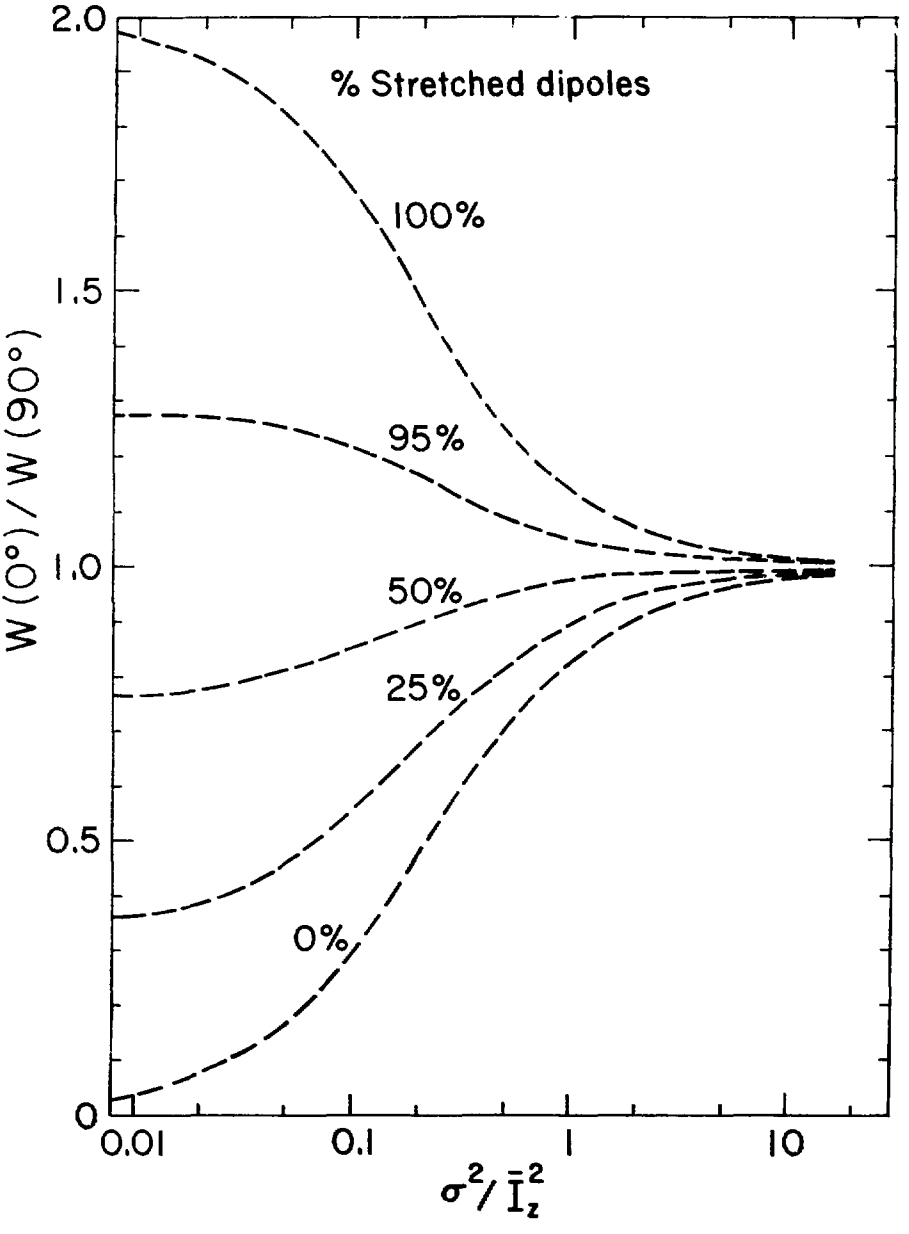

XBL 807 1673

Fig. 24a

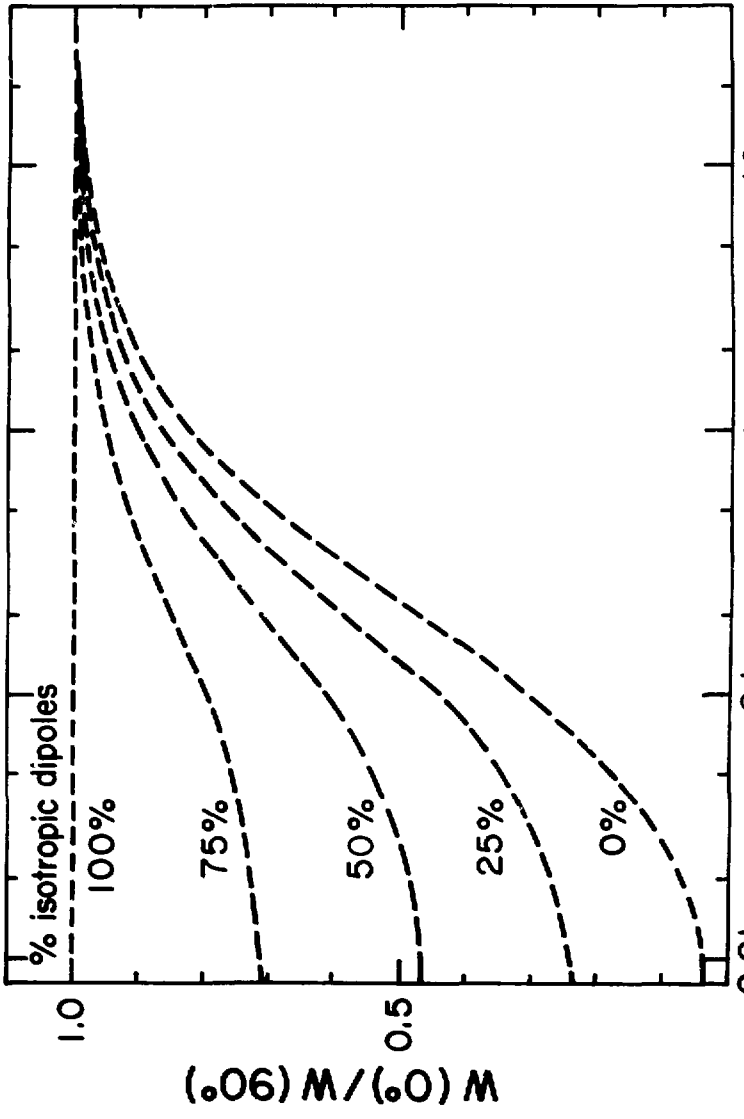

XBL 807-1671

Fig. 24b

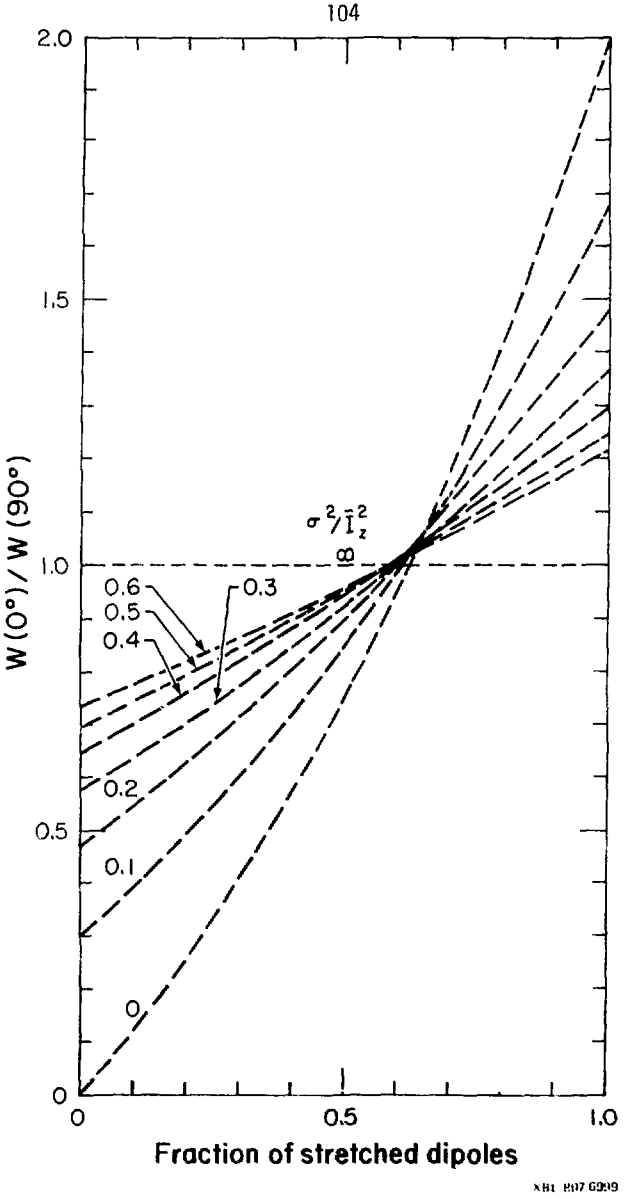
2.0
1.5
1.0
0.5
0
0
0.5
1.0
W (0°) / W (90°)
Fraction of stretched dipoles
$\sigma^2/\bar{I}_z^2$
∞
0.6
0.5
0.4
0.3
0.2
0.1
0
XBL 807 6939

Fig. 25a

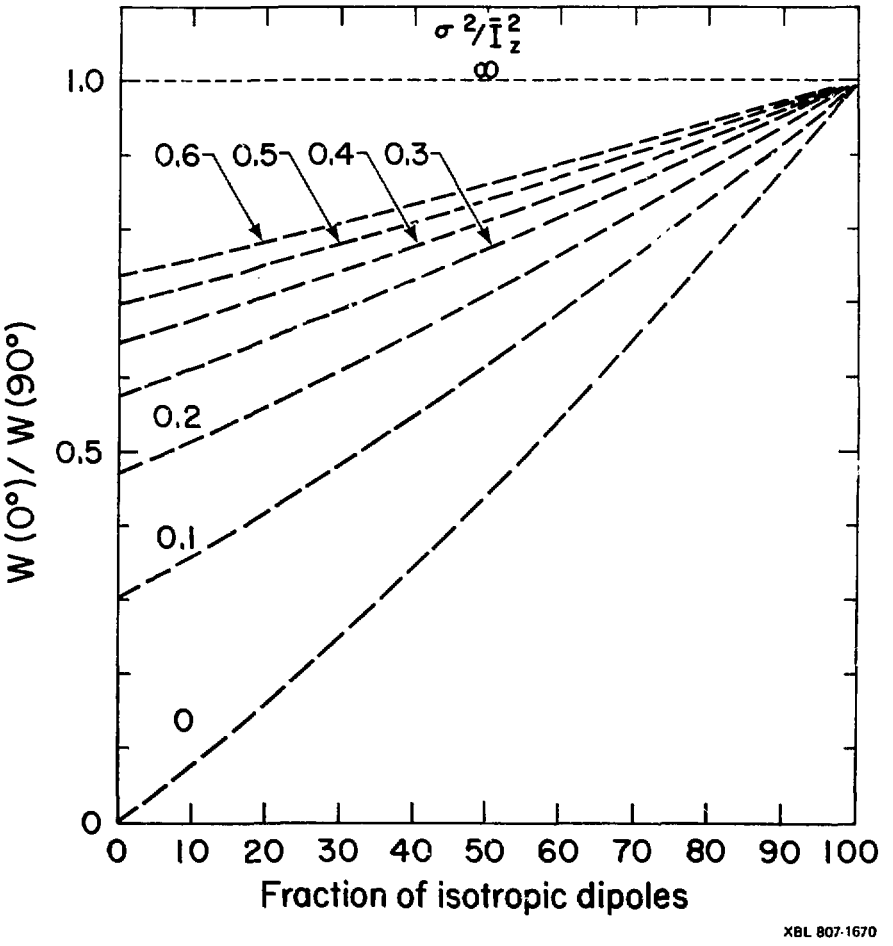
$\sigma^2/\bar{I}_z^2$
∞
0.6
0.5
0.4
0.3
0.2
0.1
0
1.0
0.5
0
W (0°) / W (90°)
0 10 20 30 40 50 60 70 80 90 100
Fraction of isotropic dipoles
XBL 807-1670

Fig. 25b

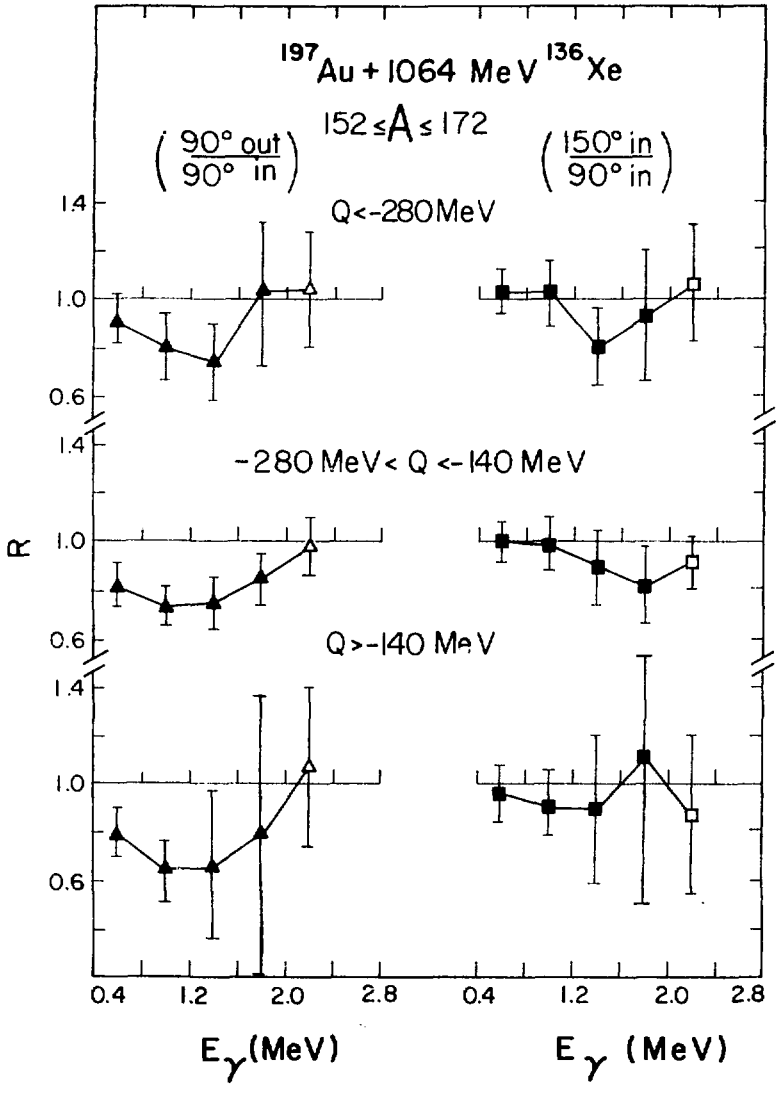

XBL 797-2298

Fig. 26

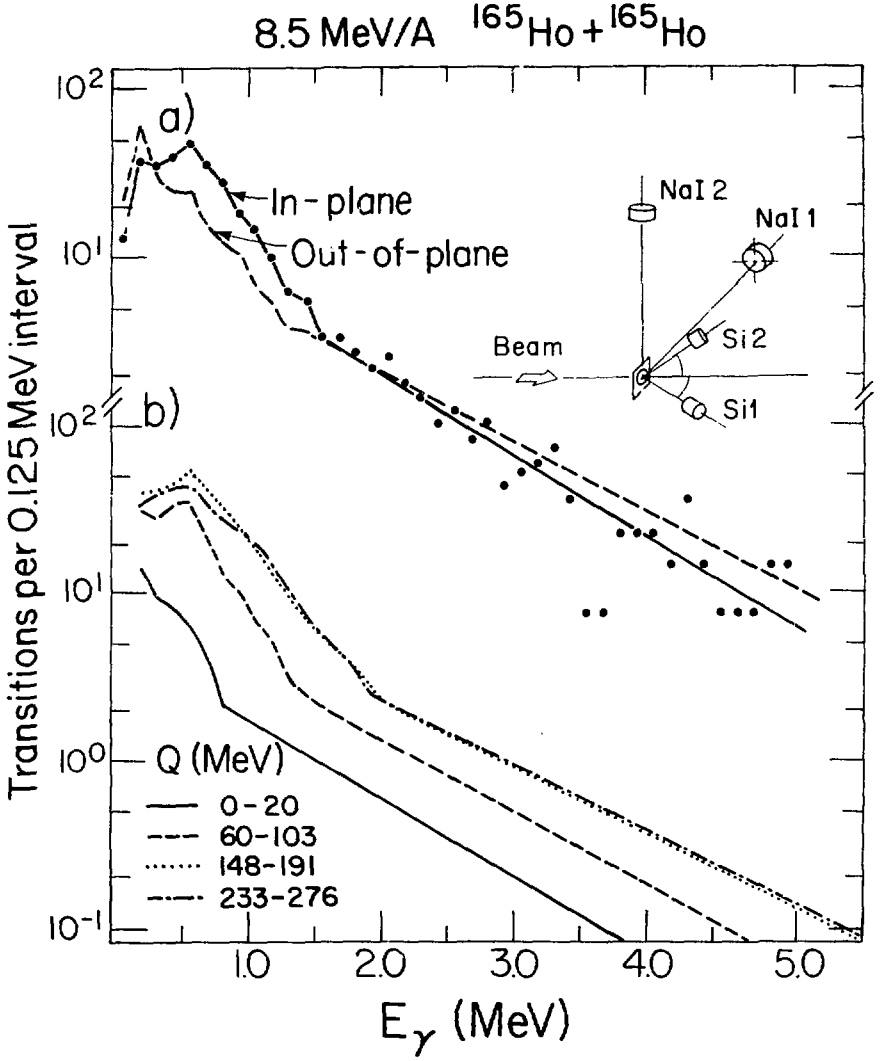

XBL 806-1194

Fig. 27

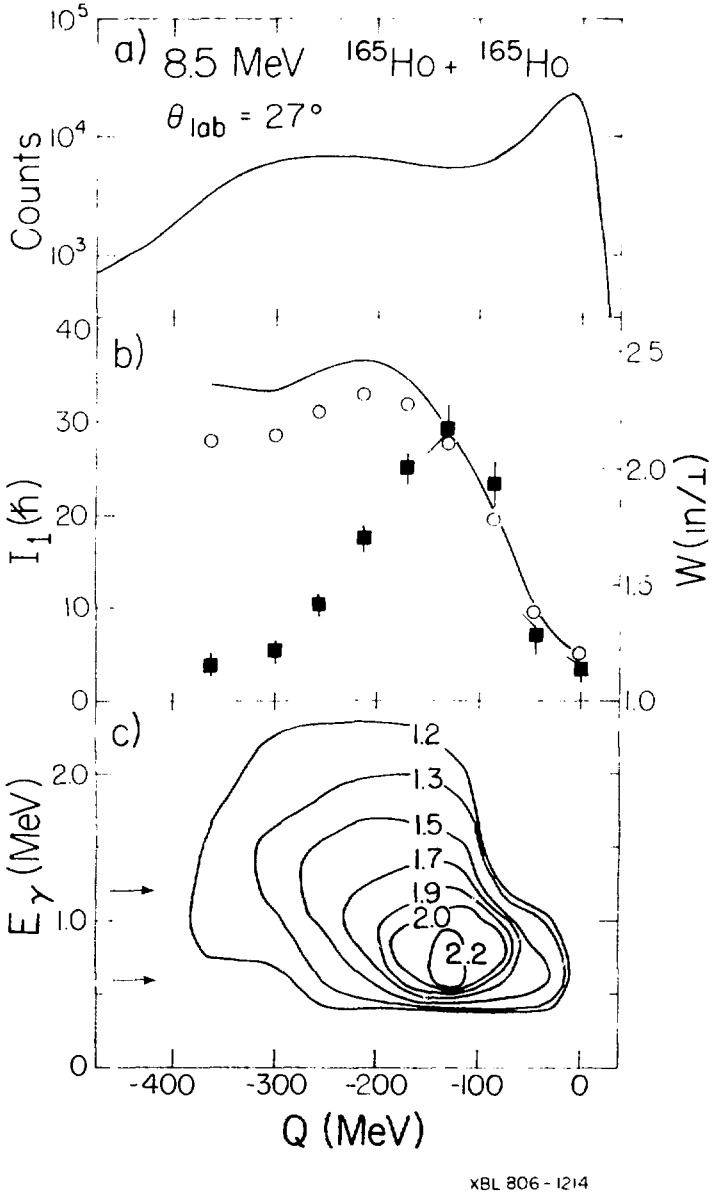
a) 8.5 MeV ^{165}Ho + ^{165}Ho
θ_{lab} = 27°
Counts
b)
$I_1(\hbar)$
W(in/⊥)
c)
E_γ (MeV)
1.2
1.3
1.5
1.7
1.9
2.0
2.2
Q (MeV)
XBL 806-1214

Fig. 28

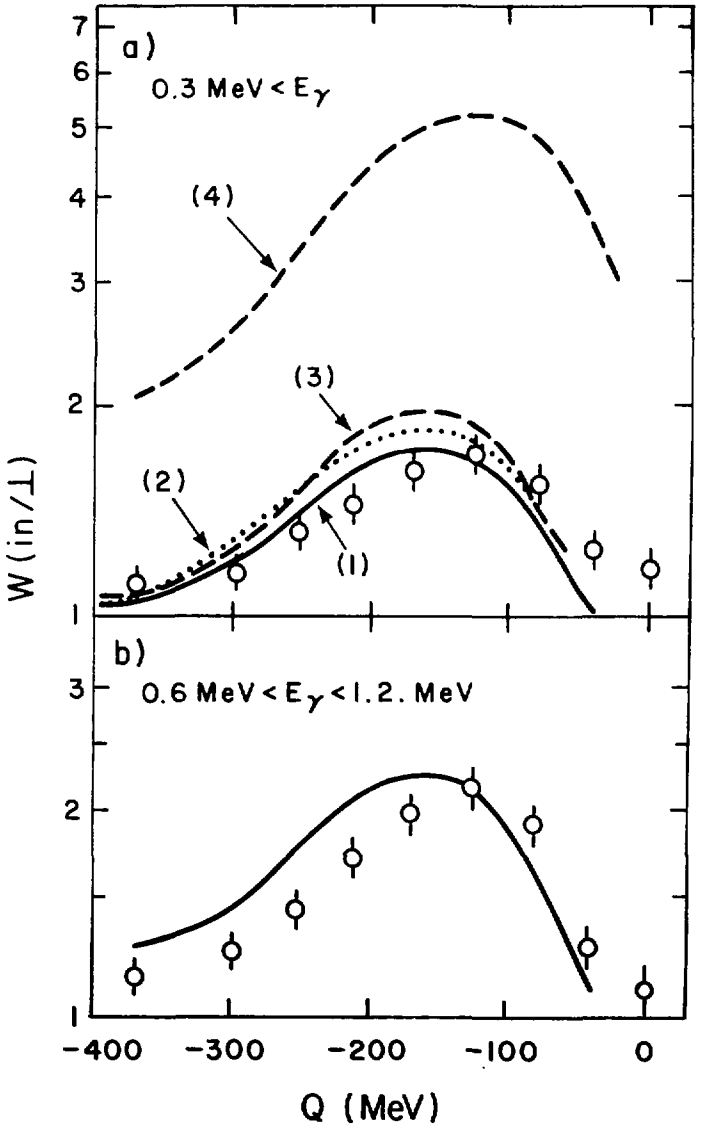

XBL806-1193

Fig. 29